NASA TECHNICAL NOTE

NASA TN D-4204

NASA TN D-4204

C. 1

SOME DYNAMIC CHARACTERISTICS OF AN ELECTRON-BOMBARDMENT ION THRUSTOR

by Eugene V. Pawlik, Shigeo Nakanishi, and Harvey R. Algeri

Lewis Research Center
Cleveland, Ohio

NATIONAL AERONAUTICS AND SPACE ADMINISTRATION • WASHINGTON, D. C. • OCTOBER 1967

NASA TN D-4204

SOME DYNAMIC CHARACTERISTICS OF AN ELECTRON-BOMBARDMENT ION THRUSTOR

By Eugene V. Pawlik, Shigeo Nakanishi, and Harvey R. Algeri

Lewis Research Center
Cleveland, Ohio

NATIONAL AERONAUTICS AND SPACE ADMINISTRATION

SOME DYNAMIC CHARACTERISTICS OF AN ELECTRON-BOMBARDMENT ION THRUSTOR

by Eugene V. Pawlik, Shigeo Nakanishi, and Harvey R. Algeri

Lewis Research Center

SUMMARY

The experimental dynamic characteristics are examined for a 10-centimeter-diameter electron-bombardment ion thrustor. These dynamics were obtained by imposing perturbations on the various input parameters while operating at the design point. Data are presented for both refractory metal and oxide-coated cathodes. The time constants associated with the cathode heater and the propellant flow were found to be significant, in some cases of the order of several seconds. Some low-frequency (100 to 1000 Hz) effects on the ion-beam current and the cathode-emission current were observed for both the discharge voltage and magnetic-field perturbations. A critical frequency phenomenon within the ion-chamber plasma seemed to exist near 400 hertz.

INTRODUCTION

Electrostatic mercury ion thrustors of various sizes and thrust capabilities for a broad range of applications have been developed and extensively reported (refs. 1 to 3). The use of these thrustors requires that they be integrated into a system including multiple arrays, power conditioning, and controls. Some array problems have been investigated and are reported in references 4 and 5. Other information is needed for the design of power conditioning and controls. The first step in such designs requires a knowledge of the steady-state control properties of the electron-bombardment thrustor, and this has been studied in references 6 and 7.

The investigation experimentally surveyed the dominant dynamic behavior characteristics of a typical electron-bombardment mercury ion thrustor. The use of dynamic characteristics permits a simplified analysis to be made of the control system by replacing all or part of a physical control system with its mathematical equivalent. A particularly attractive feature of such an analysis is that many characteristics of a com-

plete control system can be determined and studied without the necessity of operating the thrustor. The knowledge of dynamic characteristics also permits the preliminary evaluation of various design-frequency power conditioning systems.

The dynamic characteristics of a thrustor are identified by the transient response of the thrustor to variations in the input parameters. This response to deliberate input variations should be distinguished from high-current transients such as arcs or breakdowns which have been considered by other researchers (e.g., ref. 8). Each of the thrustor input parameters is examined in turn and the effects on the thrustor output are measured.

APPARATUS

Thrustor

Figure 1 shows a cutaway sketch of the electron-bombardment ion thrustor used in this study. This thrustor is identical to the one studied in reference 6. The thrustor operation may be described as follows. Liquid mercury is vaporized in a steam-heated vaporizer and delivered to the thrustor through a distributor into the ionization chamber, where it is bombarded by electrons and ionized. The ionization chamber consists of a cathode and a cylindrical anode mounted within a cylindrical enclosure, one end of which is a perforated metal screen. An electromagnet provides an axial magnetic field within the ionization chamber that tends to confine electrons emitted by the cathode within the chamber and increases their probability of collision with the neutral-mercury vapor. These collisions create a plasma within the chamber. The ions within this plasma diffuse to the screen, where they are extracted by an electric field established between the screen and the accelerator to become the ion beam. The accelerator is a second perforated plate with the holes matching those in the thrustor screen. The total accelerating voltage is applied principally between the two plates, with the accelerator voltage slightly more negative than the value necessary to prevent electron backstreaming through the accelerator holes. The net accelerating voltage is applied to the anode. (Voltages on the accelerator and anode are measured with respect to ground, which would correspond to the potential of space on an actual mission.)

Two types of orifices were used in this study to regulate propellant flow. One such orifice was a fixed diameter hole as reported in previous studies (e.g., refs. 2 and 3). The other was a variable orifice that consisted of a slit, the open area of which could be changed by the rotation of a cam. A photograph of the variable orifice is shown in figure 2. A cam to produce a step change in propellant flow can be seen in the figure. Calibration of the variable orifice was obtained at each area setting by a propellant

2

weight inventory before and after a 10-hour operating period.

The thrustor was operated with both oxide-coated and tantalum cathodes. The tantalum cathode was a single strand of wire 0.037 centimeter in diameter and 3.75 centimeters long. The coated cathode was a tantalum ribbon with a coating of barium oxide. The construction of this type of cathode is described in detail in reference 9. The anode of the thrustor was 10 centimeters in diameter and 7.6 centimeters long. The 0.130-centimeter-thick molybdenum accelerator and screen were match-drilled with 0.476-centimeter-diameter holes arranged in 0.635-centimeter equilateral triangles.

Electrical Systems and Instrumentation

The external connection diagram of the power supplies and electrical metering system of the thrustor are shown in figure 3. The supplies for energizing the magnetic-field winding, heating the cathode, and establishing the discharge voltage may be considered internal in that they supply power at voltages that are relative to the anode of the thrustor.

Operation of the thrustor to study the dynamic characteristics required a modification of the usual electrical hookup so that perturbations could be introduced into the system. Electronic modulators were used to generate these perturbations at the thrustor input parameters. The types of modulating methods employed are illustrated in figure 4. The principle of operation for all the units was similar, inasmuch as a signal from the function generator was amplified and applied to the series control element. The function generator signal was then mixed or modulated with the direct-current voltage level at the thrustor parameter by the series control element thus producing the necessary input perturbations. The frequency range of perturbations was variable from 0.01 to 1200 hertz. The amplitude of perturbations was adjustable from 0 to 50 percent of the parameter direct-current voltage.

Some effort was necessary to reduce the ripple content present in the various power supplies. Ripple reducers, which attenuated the ripple by a factor of 100, were added to the cathode heating power supply and anode power supply. A regulated low ripple power supply was substituted for the unregulated direct-current supply normally used for the discharge voltage. These modifications reduced the ripple to below 10 percent of the signal levels of the perturbations. The regulated discharge voltage supply also eliminated interference with the dynamic response that might have been produced by discharge voltage variations with both load and line changes.

Some modifications were also necessary to provide cathode-emission-current read-out and constant emission operation. These changes are shown schematically in figure 5. Operation with a constant emission current was achieved by sensing the emission

3

current and automatically adjusting the cathode heating current (with the series control element) until the desired emission current was obtained (fig. 5(a)).

The technique used to obtain the oscilloscope waveforms of the emission current responses for the various input variations is illustrated schematically in figure 5(b). The differential amplifier and matched set of voltage dividers canceled out any common mode voltage variations in the sampled emission current signals. Measured frequency response was flat (within 0.4 dB) to 1200 hertz with zero phase shift to 800 hertz and with a maximum phase shift of 30° at 1200 hertz. Variation of anode voltage of up to 500 volts had negligible effect on the emission readout.

Similar techniques were used to read out the induced fluctuations in the cathode-heating current, magnetic-field current, and the discharge-chamber voltage.

An ion-beam collector was the most suitable method for accurately determining the ion current during transient testing. Beam current measurements made at the ground return meter location (shown in fig. 3) were obscured by noise and alternating-current ground return loops through the power supplies. The collector used for this study was 1.2 meters in diameter and was located 1 meter downstream of the thrustor. The collector was connected to ground through a 5-ohm resistor across which oscilloscope measurements of the beam current were obtained. Calibration at steady-state conditions showed the collector beam current to be equal to the beam current as measured by the ground return meter.

Facility

The ion thrustor was mounted in a 20-inch-diameter (51-cm-diam) bell jar that was evacuated through a 12-inch (30-cm) valve into a 5-foot-diameter (1.5-m-diam) by 16-foot-long (4.9-m-long) vacuum tank. Figure 6 shows the thrustor and vacuum-tank installation. The tank has four 32-inch (81-cm) oil-diffusion pumps feeding into a common ejector pump, which was followed by a mechanical pump. A cryogenically cooled condenser was used to aid the vacuum pumps. The tank was normally evacuated to approximately 7×10^{-7} torr and the bell jar to 6×10^{-6} torr. When the ion thrustor was operating, both tank and bell jar pressures rose to approximately 4×10^{-6} and 1×10^{-5} torr, respectively.

PROCEDURE

The thrustor used in this study was designed to produce a 0.125-ampere mercury ion beam at a specific impulse of 4000 seconds. Most of the data were therefore obtained

in the neighborhood of these conditions. The thrustor parameters are listed in the following table for normal operating conditions with refractory metal and oxide-coated cathodes.

Thrustor parameters	Refractory metal cathode	Oxide-coated cathode
Anode voltage, V_i, V	2500	2500
Accelerator voltage, V_a, V	-625	-625
Discharge voltage, ΔV_i, V	50	35 to 25
Propellant utilization efficiency, η_u, percent	80	80
Magnetic-field intensity, B, T	3×10^{-3}	3×10^{-3}
Cathode-emission current, J_e, A	1.5	3.0
Ion-beam current, J_b, A	0.125	0.125

All data were obtained without a neutralizer which might mask other effects by providing a copious source of backstreaming electrons at certain operating conditions. The normal operating conditions were established at a constant value of $V_i/(V_i + |V_a|) = R$, the ratio of net-to-total accelerating voltage. (All symbols are defined in appendix A).

A block diagram representing the thrustor inputs, ion-beam current, and their interrelations with the thrustor components is shown in figure 7. The dynamic characteristics were generally determined by modulating one input parameter at a time while holding the others constant. Direct-current operating levels of the constant inputs were obtained from panel meters. The waveforms of the modulated input, thrustor beam, and emission current were recorded on a dual beam oscilloscope. The dynamic response to the input variations was observed for both the refractory metal and the oxide-coated cathodes.

RESULTS AND DISCUSSION

Method of Data Presentation

The dynamic characteristics of the ion thrustor are primarily described in terms of the steady-state gain and the frequency-dependent properties of the system. In theory, the dynamic behavior of any physical process can be described by an appropriate set of differential equations. The solution of the equations, even with electronic computers, is often a difficult and lengthy task. Techniques such as linearization of the existing equations can generally provide solutions which are adequate descriptions of the process behavior.

The transfer function, which defines the input-output relation of a process, is a useful concept in representing process characteristics. The nonlinear nature of most processes does not preclude the usefulness of the transfer function concept because, for small deviations about a steady-state operating point, the output-input response can be considered linear. As stated in reference 10, the transfer function can be written in Laplace transform notation as

$$\frac{O(s)}{I(s)} = KG(s)$$

where O is the output or response to an input I, K the steady-state or static gain of the system, and $G(s)$ the frequency-dependent property of the system. The term $G(s)$ when derived mathematically from the process equations is usually a quotient of two polynomials in the complex variable s. When the complex frequency $j\omega$ is substituted for s, the term $G(j\omega)$ varies in magnitude and phase angle as a function of frequency. A more detailed development is presented in appendix B.

The transfer function concept is particularly useful in the mathematical representation of a process for which the governing differential equation is unknown. The experimental observation of the output response of a process to either a sinusoidal input over a range of frequency or a small step change in input yields information which completely characterizes the system under test. Information thus obtained permits the determination of the system transfer function without the use of differential equations.

In the discussion that follows, the beam current output and dynamics associated with each input variable are investigated. The effects of variations in each of the input variables are examined in this order: neutral flow rate J_n, cathode-heating current J_f, magnetic-field intensity B, discharge voltage ΔV_i, accelerator potential V_a, and anode potential V_i.

Noise Measurements

In determining the dynamic characteristics of the thrustor, it was found that a noise level existed on the cathode-emission current and the beam current. These noise levels, which do not affect the thrustor dynamics, were present on all oscilloscope traces and varied with thrustor operating conditions.

The frequency spectrum of noise was broader than that of the imposed perturbations. The noise amplitude in some instances was considerable but not sufficient to preclude a good estimate of the response signal amplitude. The variation of noise level as a function of the various operating parameters was determined to show regions of operation

6

wherein the signal to noise ratio might be unfavorable. It is believed that the noise is generated primarily by oscillations within the discharge plasma. Typical oscilloscope waveforms of the noise measurements are presented in figure 8 for a tantalum wire cathode. Frequencies in the range of 500 to 5000 hertz were observed in the emission current, while the beam current contained frequencies up to 10 000 hertz. The amplitudes of emission and beam current noise levels with variations in propellant utilization, discharge voltage, and magnetic field are presented in figures 9 to 11 for a refractory metal cathode. Noise amplitudes increased with propellant utilization as the cathode temperature was increased. The beam current noise also tended to increase with increasing magnetic-field strength or decreasing discharge voltage. Both of these conditions retarded the flow of electrons in the anode.

The noise levels for an oxide-coated cathode were also observed and, in general, substantiated the trends noted previously for the refractory cathode. The amplitude of the noise, however, was considerably greater with the oxide-coated cathode. For example, noise amplitude of 0.7 ampere on the emission current and 0.035 ampere on the beam current were observed when the thrustor was operating at normal conditions. These noise amplitudes were approximately one to two orders of magnitude greater than those observed when the refractory metal cathode was used.

Propellant Flow

The responses of the exhaust-beam current and the cathode-emission current to a step change in propellant flow were studied. Thrustor dynamics with respect to propellant flow were established for both a refractory metal and an oxide-coated cathode which were used in the ion source. For these tests, the thrustor was operated with the variable orifice stopped down to 0.161-ampere equivalent flow. A 20-percent step increase in flow rate was introduced to the ion source as the orifice was opened. Manual operation of the orifice cam provided propellant flow rise times on the order of 0.02 second. The effect of the abrupt change in flow rates on the internal vapor pressure of the vaporizer was assumed to be small since a large mercury surface was maintaining the equilibrium vapor pressure and the volume of the vaporizer chamber was substantial. In general, an increase in the propellant flow increased the ion-chamber plasma density which results in both an increased extraction of ions and a greater emission current.

Numerous inputs besides propellant flow rate affect thrustor operation. The block diagram of the cathode and thrustor in sketch (a) helps show the interrelation of the thrustor components and operational parameters.

7

Manifold

$\frac{K_1}{1+\tau_1 s}$

J_n

n

K_2

B ΔV_i

J_b

B ΔV_i B ΔV_i

K_6 J_e K_3

T

Cathode

$\frac{K_4}{1+\tau_4 s}$

ΔV_i

J_f

$\frac{K_5}{1+\tau_5 s}$
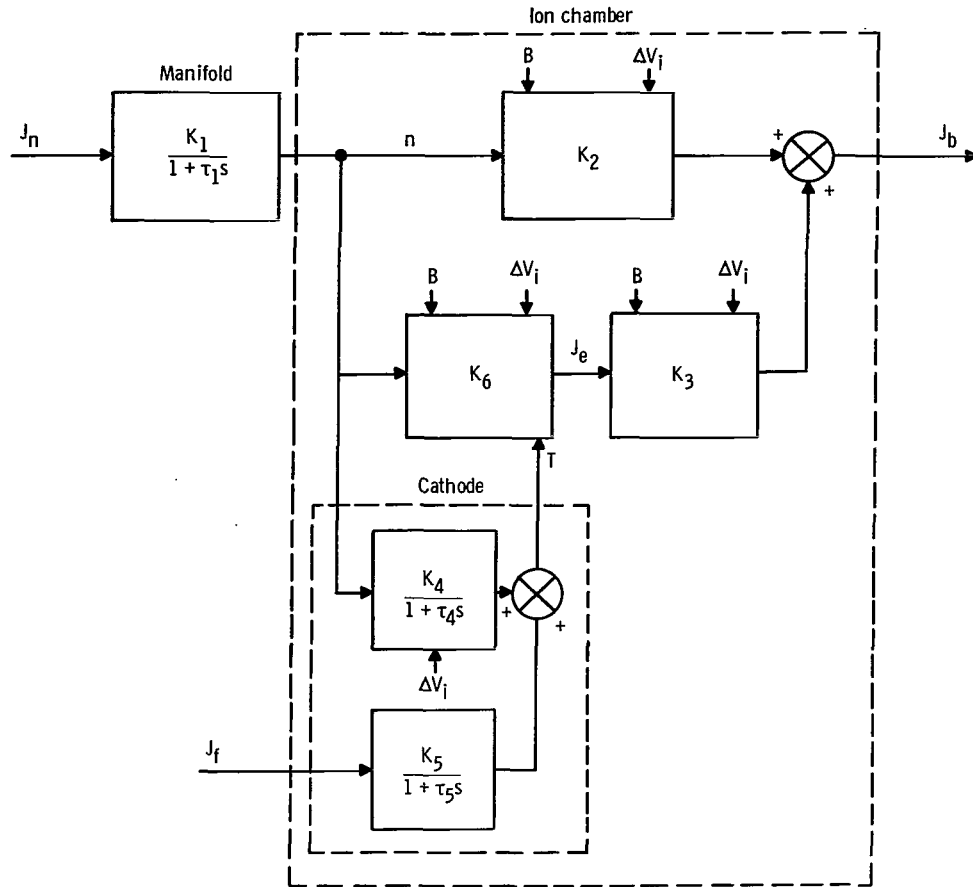
(a)

This diagram, which is more specific than the general block diagram of figure 7, relates the beam current J_b to the thrustor inputs, propellant flow J_n and cathode heating current J_f. Each gain in the system is represented by K and the time constants by τ with a first-order transfer function of the form $K/(1 + \tau s)$. The dependence of the thrustor gains on magnetic-field and discharge voltage is shown as additional inputs to the blocks affected. The frequency dependence of these terms is not included in this sketch. The dynamic characteristics attributable to the propellant flow passage or manifold are shown external to the ion chamber.

The values of K_1 and τ_1 are primarily functions of the thrustor geometry and the thermal velocity of the propellant vapor. The value of K_1 may be estimated from molecular flow calculations. The time constant τ_1 as obtained from the response curves was about 0.035 second. This is in the range (from 0.022 to 0.057 sec) given by the dominant root τ' calculated in appendix C.

8

The gain K_2 is indicative of propellant utilization at constant emission current operation, and K_3 relates the beam current output to the emission current at a constant rate of propellant input. The gain K_6 relating emission current to number density n and cathode temperature T is difficult to define. For a given cathode geometry, it is possible to approximate this block by a gain term relating emission to propellant flow at a constant discharge voltage and cathode-heating current.

The cathode thermal capacity and the effect of cathode heating due to ion bombardment are internal to the ion chamber, and they are shown by the blocks which comprise the cathode. The effect of ion-bombardment heating is represented by K_4 and τ_4. These characteristics are largely dependent on the cathode type as will be shown in the subsequent sections. Electrical heating of the cathode by the current J_F is represented by K_5 and τ_5 and will be discussed in the section Cathode-Heating Current.

Refractory metal cathode. - Typical response curves for a tantalum cathode are presented in figure 12 for low, normal, and high values of discharge voltages. The discharge voltage changed the steady-state gain but had no noticeable effect on the response times. Both the beam and emission current increased with an increase in propellant flow rate exhibiting a first-order response to the abrupt change in propellant input. Both increases in beam and emission currents with flow rate were attributable to an increased ion density at higher propellant flows. This increased density would result in greater extraction at the accelerator grids as described in reference 11. It is felt that the increased ion density and the increased ion current falling on the cathode reduced the space charge and provided additional cathode heating, thus increasing electron emission (ref. 12). The gains K_2, K_3, and K_4 varied with the electrical parameters, particularly the discharge voltage, as reflected by the curves in figure 12. For operation at 80-percent propellant utilization, a value of 0.042 for K_3 was determined from reference 6.

The range of variation in the various gains is shown in figures 13 to 15. The magnitudes of the beam-neutral flow gains as functions of the discharge voltage, magnetic-field strength, and propellant utilization efficiency were consistent with those reported in reference 6.

Figure 16 presents the beam response to neutral flow with an emission controller in the circuit. For this constant emission current operation, the beam current to neutral flow transfer function is simply $K_1K_2/(1 + \tau_1 s)$. Comparison of figures 12 and 16 shows that in either case the nature of the beam current response was similar.

The dead time (time between input change and change in response at collector) of the response traces was small with respect to the time constants of the thrustor. The

factors contributing to this dead time are the thermal velocity of the propellant between the orifice and the plasma, the ion drift time through the plasma, and the time of flight from the accelerator to the collector. For a vapor temperature of 100° C, the thermal velocities are of the order of 180 meters per second. The drift velocity of the ions through the plasma was not easily calculable but was assumed to be sufficiently high so that its contribution to the total dead time was negligible. The time of flight for an accelerating voltage of 2500 volts for the 1-meter distance to the collector is 20 microseconds. The calculated dead time on the basis of the previous assumptions was about 2 milliseconds. This dead time was checked experimentally by recording the orifice cam position and beam current at the collector simultaneously. These results are presented in figure 17. The cam was turned slowly to establish the open and closed positions as determined by the beam levels. These traces are shown in figure 17(a). The orifice was then opened rapidly as shown in figure 17(b). Dead times within these traces appear to be about 2 milliseconds.

Oxide-coated cathode. - The ion source was operated with an oxide-coated cathode and the beam and emission current response were obtained. The change in propellant flow in this case, however, produced sizable changes in the thrustor output. These changes were probably caused by either emission heating (joule heating of emission current through oxide layer) or ion-bombardment heating, effects which were only slightly noticeable for the refractory metal cathode. The component of the block diagram containing K_4 and τ_4 is therefore significant with the oxide-coated cathode. The steady-state characteristics also varied significantly from those of the metal cathode. The maximum value of beam current that could be obtained by an increase in the cathode-heating current varied inversely with the discharge-chamber voltage. The steady-state characteristics are plotted as beam current against cathode-emission current for various values of discharge-chamber voltage ΔV_i in figure 18 for neutral-flow rates of 0.161 and 0.192 ampere equivalent flow rate corresponding to the orifice open and closed positions. A condition was reached for each of the two flow rates where the cathode was heated sufficiently by both ion bombardment and the ohmic heating of the emitted current and, therefore, the cathode-heating current was not necessary. The cathode-heating current under these conditions could not be used to control the emission current; therefore, the only effective control of the beam current was the discharge voltage. The discharge voltage at which heating current was unnecessary was noted to be a function of chamber plasma density, being lower at high densities. The response of an oxide cathode at a 35-volt discharge-chamber voltage is presented in figure 19. The step change was repeated and the response traces were obtained for two time scales. The initial response in either case (due to the propellant increase) was identical to that observed for the refractory cathode. The prevailing time constant with the oxide-coated cathode, however, was due to the emission or ion-bombardment heating and was quite

long (about 2.8 sec at ΔV_i = 35 V), and increased as the discharge voltage increased. The thrustor response for higher discharge voltages is presented in figure 20. The initial and final values for the response curves are indicated by solid symbols in figure 18(a) and (b), respectively.

Although the time lag was small for the majority of the data presented, two conditions were encountered where this lag became significant. The response for these cases are both presented in figure 21. These cases represent a step change into a region where the ion bombardment is increased. The increased bombardment could result in an increase in cathode temperature and increased activation which would lead to higher emission. The increased emission would result in greater emissive heating which would also increase cathode temperature. Thus, the initial rapid rise is followed at a later time by another rapid rise as the emission heating brings the cathode near the temperature necessary for an uncontrolled discharge or arc. The cathode in both of these cases was probably in a deteriorated condition where the majority of the barium on the surface was depleted. Increased bombardment could be responsible for increased activation and increased emission.

Cathode-Heating Current

The response of the exhaust beam current and the cathode-emission current were observed with a refractory and an alkali earth-coated cathode as small perturbations were applied to the direct-current cathode-heating level. A fixed orifice which provided mercury at a 0.161-ampere equivalent flow rate was used for these and all subsequent tests.

Refractory metal cathode. - Sinusoidal variations were imposed on the cathode-heating current over a range from 0 to 1000 hertz as the thrustor operated near normal conditions. Wave forms were recorded on an oscilloscope for the cathode-heating, emission, and beam currents. The heating current modulations were kept at less than 5 percent of the direct-current level for these tests. The frequency response of the beam and emission currents to the cathode-heating current were constructed from the oscilloscope waveforms and are presented in figures 22 and 23. The cathode exhibited the properties of a first-order thermal system at low frequencies. The breakpoint frequency $(1/2\pi\tau)$ was 0.8 hertz. When a simple model of the cathode (appendix D) was used, the calculated breakpoint frequency was 0.6 hertz. In view of the unknown validity of assumptions such as cathode temperature and active emissive area, the agreement is considered good.

The analysis shows that the breakpoint frequency varies directly as the third power of the cathode temperature. Small changes in cathode temperature from the assumed

value of 2400° K could therefore bring the breakpoint frequency into closer agreement between theory and experiment. The leveling off of amplitude ratio or the departure from the straight-line portion of the calculated curve at higher frequencies was not predicted by the theoretical curve. Thermal response is sufficiently attenuated at the higher frequencies so that cathode temperature fluctuations can be neglected. The perturbation in the cathode-heating current imposes about a 0.3-volt variation across the cathode. The average discharge voltage is thus perturbed by 0.3 volt, but this perturbation amplitude is not considered sufficient to account for the observed deviation of the attenuation curve from that expected for a first-order lag system.

The phase response of the beam and the emission currents to cathode-heating current is shown in figure 23. Both responses were defined by essentially a single curve over the frequency spectrum of the test. The beam and emission currents were therefore always in phase with each other.

The beam current and the emission current lagged the filament heating current as would be expected of a thermal system. The experimental trend followed the theoretical first-order response up to about 10 hertz. At higher frequencies, the experimentally obtained phase lag continued to increase beyond 90° characteristically as in a higher order system.

Oxide-coated cathode. - Beam and emission current response to cathode-heating current was studied by using the barium oxide-coated cathode. Because the response was observed to be quite long, a low frequency square wave from the function generator was used to examine the dynamic characteristics. Typical emission response curves are presented in figure 24 for both a step increase and decrease in cathode heating current. Both the beam and emission response characteristics were essentially unchanged over a wide range of thrustor operating regions. The response curves all indicated an abrupt initial jump. Observation of beam and emission current responses to step changes in discharge voltage showed the same effect. A nonlinearity was observed in the response of the beam and emission current inasmuch as the decreasing heating current produced a different response from that of an increasing current. A decreasing current produced a first-order response with a time constant of about 2.8 seconds. An increasing current produced a first-order response with a time constant of about 1 second.

Magnetic Field

The beam and emission currents were observed for a refractory cathode as small perturbations were applied to the magnetic-field current. The frequency response for both the emission and beam currents is presented in figure 25. The response for the

emission current was flat up to 100 hertz after which it dropped off as a first-order system (fig. 25(a)). The beam current response was flat up to the vicinity of 100 hertz where it exhibited a slight rise (fig. 25(b)). It then dropped off sharply reaching a minimum at about 400 hertz after which it increased. The phase angle between the magnetic field and the beam and emission currents is presented in figure 26. The phase angle between the field and both emission and beam currents was zero up to 100 hertz. A large shift in phase occurred between 200 and 500 hertz resulting in a phase lag of about 300°.

The thrustor dynamics for the magnetic-field perturbations cannot be represented simply by a linear system approximation. In addition, data at higher frequencies would be desirable in order to obtain a more complete system representation. An examination of the data seemed to indicate that some loss or energy absorption process within the plasma existed near 400 hertz. An ion-cyclotron frequency was calculated to be 250 to 416 hertz for a magnetic-field intensity which varied from 3×10^{-3} to 5×10^{-3} tesla along the axis of the thrustor. It is particularly interesting that the observed phenomenon occurred near the ion-cyclotron frequency because collisions of large mass particles such as ion-ion or ion-neutral would be expected to damp out periodic motion of the ions. An oscillation, however, has been found to exist (ref. 13) in a cesium plasma column at frequencies near the ion-cyclotron frequency.

A loading effect on the magnetic-field power supply was noted at all of the direct-current levels of field strengths investigated. At each level, the magnetic-field perturbations were distorted considerably from that of a sine wave in the vicinity of 200 hertz. Quenching the plasma by reducing the discharge voltage to zero eliminated the distortion in the field solenoid current. Typical results for a field of 3.0×10^{-3} tesla are presented in figure 27. These and other effects associated with perturbation frequencies in the neighborhood of the ion gyrofrequency are in themselves interesting plasma-related phenomena. Detailed analysis or experimentation was not pursued because it would have represented a substantial increase in the scope (and length) of this investigation.

Discharge Voltage

Both refractory metal and oxide-coated cathodes were investigated as the discharge voltage was modulated. Sinusoidal perturbations were used over a frequency range from 0.1 to 1000 hertz.

Refractory metal cathode. - Data were obtained at a discharge voltage of 45 volts with a 10-volt peak-to-peak amplitude perturbation. The beam and emission current responses were obtained and are presented in figures 28 and 29. The beam current to discharge voltage amplitude ratio was flat to 100 hertz. A very pronounced dip in the

amplitude-frequency response curve occurred at 400 hertz indicating, as in the case of the magnetic-field perturbations, the possible existence of an energy absorption process within the plasma with a critical frequency near this value. The emission current, however, increased in amplitude in this region, the amplitude-frequency suggesting a lead network. The phase angle between the input and outputs increased with increasing frequency for frequencies above 10 hertz.

Oxide-coated cathode. - The data obtained for the refractory metal cathode was also obtained for an oxide-coated cathode. The response for the beam and emission current at two values of discharge voltage (25 and 35 V) is presented in figures 30 and 31. The perturbation amplitude was about 6 volts peak to peak. The amplitude-frequency response curves for the beam current were similar to those obtained for the refractory cathode with the critical point not as sharply defined. The emission response curve, however, varied considerably from that of a refractory metal cathode and further varied with the direct-current levels of the discharge voltage. The amplitude continuously decreased with frequency at discharge voltage of 35 volts, while it followed the ion-beam response for a discharge voltage of 25 volts. A large increase in phase lag (fig. 31) was again noted for both beam and emission currents. The lack of similarity in the emission current response characteristics of the refractory metal and of the oxide-coated cathodes as contrasted to the similarity in the beam current responses is difficult to explain because emission and beam currents are usually in phase. More definitive diagnostics within the plasma itself can possibly give a better insight into the mechanism which yields the observed response characteristics.

Accelerator Potential

Sinusoidal perturbations were introduced on the accelerator potential over a range from 0.1 to 1200 hertz. Typical waveforms obtained during this testing are presented in figure 32. The ratio of the amplitude of both the beam and emission current to the amplitude of the accelerator potential modulation was noted to be constant over this range of frequencies. The anode voltage, discharge voltage, and magnetic-field strength were kept constant during this part of the study. The ion extraction effect of the accelerator potential on the plasma can be seen in the beam current response waveform as shown in figure 32(a). A phase shift of 180° exists between the two signals since the greater negative voltage represents the higher extraction voltage. The beam current and emission current response for the same accelerator potential variation are presented in figure 32(b). A slight effect on the emission current (0.08 mA/V) can be noted. The emission current appeared to be in phase with the accelerator potential. The variations in emission current are apparently due to a slight change in ion density within the

chamber plasma as the extraction rate was varied.

A noteworthy effect was observed as the direct-current level of the accelerating potential was raised. A condition was eventually reached, as shown in figure 32(c), where electron backstreaming occurred along the ion beam because of an insufficient potential barrier for a portion of the sine wave cycle. As this condition was reached, an increased ion-beam current as measured by the collector was noted and was observed to increase as the accelerator voltage was increased. This increase in measured collector current represents the increased quantity of electrons supplied to the beam plasma to alleviate the deficiency due to the backstreaming electrons. It appears, therefore, that an effective method of measuring the exact voltage necessary to prevent backstreaming can be provided by the accelerator voltage perturbation technique. The accelerator voltage at which backstreaming occurred as measured by this method (see fig. 32(c)) is 620 volts.

Anode Voltage

The anode voltage was varied with 1000-volt peak-to-peak sinusoidal perturbations while operating at a direct-current level of 2500 volts. The beam current amplitude ratio was about 1.3×10^{-5} ampere per volt, and no variation from this value was evident in the range of frequencies investigated (0.1 to 1200 Hz). The emission current amplitude ratio, however, was observed to increase at higher frequencies. These results are presented in figure 33. The beam current remained in phase with the input signal and the emission current was always 180° out of phase.

It is not understood why the beam current response was unaffected in spite of the significant change in emission current response. The accuracy and stability of the emission current readout amplifier circuit were verified by a fixed-resistive-load calibration test. Also, the observed responses to magnetic-field and discharge-voltage perturbations have shown the emission readout to register attenuation as well as amplification.

The changing character of the noise, which appeared in the emission current signal as the driving frequency was varied, showed that the plasma was affected. It is felt that plasma diagnostics beyond the scope of the present investigation may be helpful in obtaining a better understanding of the observed results.

CONCLUDING REMARKS

Some dynamic characteristics of a 10-centimeter-diameter electron-bombardment

ion thrustor were determined experimentally. The propellant chamber pressure and cathode temperature (i. e., cathode emission) responses were essentially first-order lags. The time constant associated with the propellant flow was about 0.035 second. The cathode time constant was about 0.2 second on a refractory metal cathode and as long as 2.8 seconds for an oxide-coated cathode.

In the cathode, there were observable effects both of direct heating and of indirect heating such as by ion bombardment and joule heating by the emitted current. The indirect heating effects were more pronounced in the oxide-coated cathode than in the refractory metal cathode.

The output response of the thrustor to sinusoidal perturbations in the magnetic field, the discharge voltage, anode potential, and accelerator potential was flat up to frequencies of about 100 hertz. There was no phase shift, and the amplitude ratio was a function of the steady-state thrustor parameters.

Above 100 hertz, frequency-dependent characteristics were observed. In particular, a form of critical frequency phenomenon within the plasma existed at about 400 hertz. Large variations in amplitude response and phase shift were obtained. Plasma oscillations and instabilities probably are a strong contributing factor to the observed phenomena. Assessing the significance of the observed dynamic behavior from the standpoint of the underlying physics and mechanisms is beyond the scope of this investigation. From a practical or applied viewpoint, though, the characteristics of the various thrustor components (whether explained or not) should be recognized when designing an integrated system. The cathode and propellant feed responses appear to be predictable and controllable. Responses attributable to plasma processes have characteristic frequencies which are near the ion-cyclotron frequency, but the designs can be adjusted to avoid these frequencies.

Lewis Research Center,
    National Aeronautics and Space Administration,
        Cleveland, Ohio, March 21, 1967,
            120-26-02-05-22.

APPENDIX A

SYMBOLS

A   cross-sectional area of ion chamber, cm^2

a   distributor flow area, cm^2

B   magnetic-field intensity, T

C_m coefficient of mth derivative of input in equation representing behavior of system (see appendix B)

C_p specific heat

c   amplitude of input

D_n coefficient of nth derivative of output in equation representing behavior of system (see appendix B)

e   electron charge, 1×10^{-19} C

G   steady-state gain

G(s)   frequency dependence term of system transfer function expressed as function of s

I(s)   system input as function of s

i(t)   system input as function of t

J_a accelerator drain current, A

J_b ion-beam current, A

J_e cathode-emission current, A

J_f cathode-heating current, A

J_i anode current, A

J_m magnetic-field current, A

J_n neutral propellant flow rate, equivalent amperes of singly charged mercury ions

$J_{n,d}$ neutral propellant flow rate through distributor, equivalent amperes of singly charged mercury ions

J_s screen current, A

J_{sd} screen-distributor current, A

j   complex number representing $\sqrt{-1}$

K   steady-state system gain

k   radiator constant

M   mass, g

n   mercury number density downstream of distributor, cm^3

n'   mercury number density upstream of distributor, cm^3

O(s)   output (response) of system as function of s

o(t)   output (response) of system as function of t

q_n heat added to cathode

q_r heat radiated from cathode

R   ratio of net-to-total acceleration voltage, $V_i / (V_i + |V_a|)$

r   cathode resistance

$\mathcal{S}$	generalized linear system	θ	phase angle difference between input and output, rad or deg
s	complex operator $\sigma + j\omega$ for Laplace transform of given function of time	ν_a	average thermal velocity of propellant flow
T	cathode temperature, $^{\circ}K$	τ	time constant, sec
t	time, sec	ω	angular frequency, rad/sec
V	thrustor volume downstream of distributor, cm^3		

$\mathcal{S}$ generalized linear system

s complex operator $\sigma + j\omega$ for Laplace transform of given function of time

T cathode temperature, $^{\circ}K$

t time, sec

V thrustor volume downstream of distributor, cm^3

V' thrustor volume upstream of distributor, cm^3

V_a accelerator potential, V

V_i anode potential, V

ΔV_i discharge voltage, V

X ratio of output-to-input amplitudes

z amount of charge on mercury ion

α cathode emissive area, cm^2

ϵ surface emissivity

η_u propellant utilization efficiency

θ phase angle difference between input and output, rad or deg

ν_a average thermal velocity of propellant flow

τ time constant, sec

ω angular frequency, rad/sec

Subscripts:

m m^{th} term in expression (see eq. (B10))

n n^{th} term in expression (see eq. (B10))

o steady state

0 initial or base point

1,2,3,4,5,6 processes in thrustor

Superscripts:

m term corresponding to m^{th} derivative of input i(t) (see appendix B)

n term corresponding to n^{th} derivative if output o(t) (see appendix B)

18

APPENDIX B

RELATION BETWEEN TRANSFER FUNCTION AND FREQUENCY

RESPONSE OF SYSTEMS

The relation between the input $i(t)$ and output response $o(t)$ for a linear system $\mathcal{S}$ can be represented by linear differential equations with constant coefficients as follows:

(b)
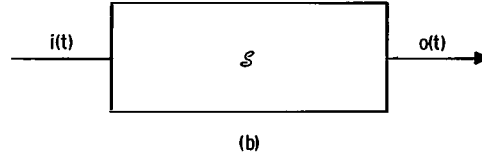
$$C_m \frac{d^m i(t)}{dt^m} + C_{m-1} \frac{d^{m-1} i(t)}{dt^{m-1}} + \ldots + C_1 \frac{di(t)}{dt} + C_0 i(t)$$

$$= D_n \frac{d^n o(t)}{dt^n} + D_{n-1} \frac{d^{n-1} o(t)}{dt^{n-1}} + \ldots + D_1 \frac{do(t)}{dt} + D_0 o(t) \qquad (B1)$$

Taking the Laplace transform of equation (B1) yields

$$\left[C_m s^m + C_{m-1} s^{m-1} + \ldots + C_1 s + C_0 \right] I(s) = \left[D_n s^n + D_{n-1} s^{n-1} + \ldots + D_1 s + D_0 \right] O(s) \quad (B2)$$

where $I(s)$ is the Laplace transform of the input $i(t)$ and $O(s)$ is the Laplace transform of the output response $o(t)$.

The transfer function $G(s)$ is defined as the ratio

$$G(s) \equiv \frac{O(s)}{I(s)} = \frac{C_m s^m + C_{m-1} s^{m-1} + \ldots + C_1 s + C_0}{D_n s^n + D_{n-1} s^{n-1} + \ldots + D_1 s + D_0} \qquad (B3)$$

where $G(s)$ is a complex quantity represented by a magnitude and a phase angle.

If the input $i(t)$ is limited to only sinusoidal excitation, the steady-state output response $o(t)$ will be a sinusoid of the same frequency. This fact stems from the following properties:

19

(1) Repeated differentiation or integration of a sinusoid yields a sinusoid of like frequency.

(2) The sum of a number of sinusoids of like frequency with arbitrary phase and amplitude yields a sinusoid of the same frequency.

For a given input of amplitude c and frequency ω,

$$i(t) = c \cos \omega t = \frac{c}{2}\left[e^{j\omega t} + e^{-j\omega t}\right] \tag{B4}$$

the response can be written as

$$o(t) = X c \cos(\omega t + \theta) = X \frac{c}{2}\left[e^{j\theta}e^{j\omega t} + e^{-j\theta}e^{-j\omega t}\right] \tag{B5}$$

where X is defined as the ratio of amplitudes of the output to the input. The angle θ is the phase angle between the output and the input.

Since $\mathscr{S}$ is linear, the principle of superposition can be applied, and the input can be considered as two separate generators $i_1(t)$ and $i_2(t)$ transferring through the system $\mathscr{S}$ to produce the two output components $o_1(t)$ and $o_2(t)$. Thus,

$$i_1(t) = \frac{c}{2} e^{j\omega t} \tag{B6}$$

$$o_1(t) = X \frac{c}{2} e^{j\theta}e^{j\omega t} \tag{B7}$$

$$i_2(t) = \frac{c}{2} e^{-j\omega t} \tag{B8}$$

$$o_2(t) = X \frac{c}{2} e^{-j\theta}e^{-j\omega t} \tag{B9}$$

Substituting the expressions for $i_1(t)$ and $o_1(t)$, along with their respective derivatives, into the differential equation given by equation (B1) and assuming zero initial conditions yield

$$\frac{1}{2}\left[C_m(j\omega)^m + C_{m-1}(j\omega)^{m-1} + \ldots + C_1(j\omega) + C_0\right]ce^{j\omega}$$

$$= \frac{1}{2}\left[D_n(j\omega)^n + D_{n-1}(j\omega)^{n-1} + \ldots + D_1(j\omega) + D_0\right]Xce^{j\theta}e^{j\omega} \tag{B10}$$

Canceling $ce^{j\omega}$ from both sides and solving for $Xe^{j\theta}$ yield

$$Xe^{j\theta} = \frac{C_m(j\omega)^m + C_{m-1}(j\omega)^{m-1} + \ldots + C_1(j\omega) + C_0}{D_n(j\omega)^n + D_{n-1}(j\omega)^{n-1} + \ldots + D_1(j\omega) + D_0} \tag{B11}$$

Comparing equation (B11) with equation (B3) shows that

$$Xe^{j\theta} = G(s)\big|_{s=j\omega} = G(j\omega) \tag{B12}$$

Equation (B12) is immediately recognized as a complex quantity whose magnitude,

$$X = \big|G(j\omega)\big|$$

and phase angle,

$$\theta = \tan^{-1} \frac{\vartheta[G(j\omega)]}{Re[G(j\omega)]}$$

are both functions of the frequency ω Similarly, substituting the expressions $i_2(t)$ and $o_2(t)$ and their derivatives into the differential equation (B1) yields

$$Xe^{-j\theta} = G(s)\big|_{s=-j\omega} = G(-j\omega) \tag{B13}$$

The quantities $Xe^{-j\theta}$ and $Xe^{j\theta}$ of equations (B13) and (B12) are complex conjugates. For each discrete value of ω, therefore, the numerical values of the X's and θ's of the two output components $o_1(t)$ and $o_2(t)$ are equal.

The complete output function as stated previously is the linear sum of the two output components. The two quantities X and θ, which characterize the output function, can be obtained directly from the transfer function represented by equation (B3). Conversely, the experimental evaluation of the amplitude ratio and phase angle between the output and the input over a range of frequencies enables the identification of the system transfer function.

The transfer function of any physical system as a function of the complex frequency ω can be obtained by exciting the system input with an incremental sinusoidal variation about a steady-state operating point and measuring the amplitude ratio and phase difference of the output and input for each value of frequency.

An alternate method of obtaining the transfer function is to impose an incremental

change in the system input. The transient input and the output response of the system are recorded and resolved into sinusoidal functions by Fourier expansion. The magnitude and phase angle of the input and output functions are then compared at each frequency to obtain $G(j\omega)$.

APPENDIX C

CALCULATION OF NEUTRAL ATOM NUMBER DENSITY RESPONSE

DUE TO PROPELLANT FLOW

The ionization process in the thrustor with neutral propellant input into a chamber containing a thermionic emitter is depicted in sketch (c).

(c)
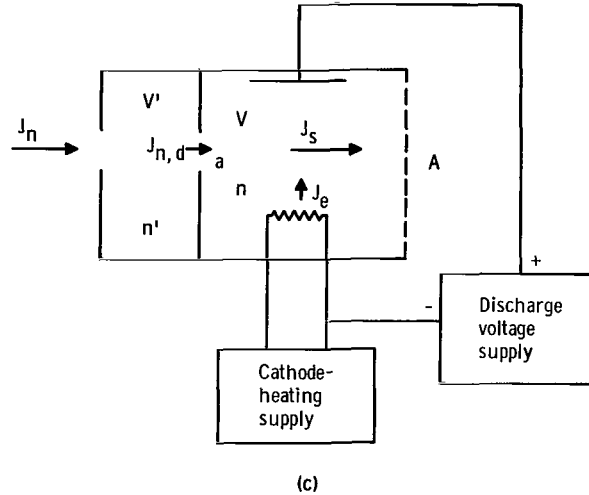
If the mean lifetime of an electron from emission to ultimate collection at the anode is negligible compared with the characteristic filling time of gaseous vapor in the chamber, the characteristic time for response in the discharge or emission current to a change in propellant flow rate can be considered to be primarily a function of vapor density within the chamber plus a correction for the cathode heating by ion bombardment.

The flow is unobstructed within the ionization chamber, but a distributor plate with an effective flow area a separates the ion chamber from the source of propellant. The effective flow area is actually comprised of a physical flow area modified by a flow coefficient factor which is a function of the flow geometry.

When a molecular flow between V' and V and a flow coefficient that does not vary with flow direction are assumed,

$$J_{n, d} = \frac{\nu_a}{4} a(n' - n)ez \qquad (C1)$$

where ν_a is the average thermal velocity of propellant flow. For the number density in V',

$$J_n - J_{n,d} = ez \frac{d}{dt}(n'V') \tag{C2}$$

where z is the amount of charge on each mercury ion. Substituting equation (C1) into equation (C2), taking the Laplace transform, and understanding that the time-dependent variables are actually perturbations on the steady-state values yield,

$$J_n + \frac{\nu_a}{4} aezn = n'\left(ezV's + \frac{\nu_a}{4}aez\right) \tag{C3}$$

For the number density in V, assuming no backflow of ions,

$$J_{n,d} - J_s = ez \frac{d}{dt}(nV) \tag{C4}$$

Substituting equation (C1) into equation (C4) and letting A be the cross-sectional area of the ion chamber yield

$$\frac{\nu_a}{4} a(n' - n) - \frac{\nu_a}{4} An = \frac{d}{dt}(nV) \tag{C5}$$

Solving for n' in the transformed equation yields

$$n' = \frac{Vsn + \frac{\nu_a}{4} n(A + a)}{\frac{\nu_a}{4} a} \tag{C6}$$

When equation (C6) is substituted into equation (C3),

$$J_n + \frac{\nu_a}{4} ezan = \frac{Vsn + \frac{\nu_a}{4} n(A + a)}{\frac{\nu_a}{4} a}\left(ezV's + \frac{\nu_a}{4}aez\right) \tag{C7}$$

Solving for J_n gives

24

$$J_n = n \left\{ \frac{4ezVV'}{\nu_a a} s^2 + ez \left[V + \left(\frac{A + a}{a} \right) V' \right] s + \frac{\nu_a}{4} ezA \right\}$$ (C8)

Then,

$$\frac{n}{J_n} = \frac{1}{\frac{4ezVV'}{\nu_a a} \left[s^2 + \frac{V + \left(\frac{A + a}{a} \right) V'}{\frac{4VV'}{\nu_a a}} s + \frac{\nu_a^2 aA}{16VV'} \right]}$$ (C9)

The time constants of the system can be found from the roots of the characteristic equation

$$s^2 + \frac{V + \left(\frac{A + a}{a} \right) V'}{\frac{4VV'}{\nu_a a}} s + \frac{\nu_a^2 aA}{16VV'} = 0$$ (C10)

Thus,

$$\tau = \frac{\frac{8}{\nu_a}}{\frac{a}{V'} + \frac{A + a}{V} + \sqrt{\left(\frac{a}{V'} \right)^2 - \frac{2a(A - a)}{VV'} + \left(\frac{A + a}{V} \right)^2}}$$ (C11)

and

$$\tau' = \frac{\frac{8}{\nu_a}}{\frac{a}{V'} + \frac{(A + a)}{V} - \sqrt{\left(\frac{a}{V'} \right)^2 - \frac{2a(A - a)}{VV'} + \left(\frac{A + a}{V} \right)^2}}$$ (C12)

The parameters of the configuration are

$$A = 78.5 \text{ cm}^2$$

$$V = 750 \text{ cm}^3$$

$$\nu_a = 2.57 \times 10^4 \text{ cm/sec for } T = 350^\circ \text{ C}$$

The value of $4a^2$ is small compared with A^2, because of the thrustor construction, and V is approximately equal to V' so that

$$\tau \simeq \frac{\dfrac{8V}{\nu_a}}{2A + 2a} \simeq \frac{4V}{\nu_a(A + a)}$$

$$\tau' \simeq \frac{\dfrac{8V}{\nu_a}}{2a} \simeq \frac{4V}{\nu_a a}$$

For a distribution area of 5.4 square centimeters,

$$\tau = 0.0015 \text{ sec}$$

and

$$\tau' = 0.022 \text{ sec}$$

and for a distributor flow area of 2.04 square centimeters,

$$\tau = 0.00152 \text{ sec}$$

and

$$\tau' = 0.057 \text{ sec}$$

The dominant time constant τ' associated with the restriction of flow through the distributor will be equal to the 0.035-second value observed experimentally in the cathode-emission response if the flow coefficient of the distributor is about 0.2. From reference 14, such a value of flow factor is reasonable.

APPENDIX D

CATHODE TRANSFER FUNCTION DETERMINATION

A simple model of the thrustor refractory metal cathode can be established for determination of the thermal transfer function. The model chosen was a cylindrical wire at a uniform temperature with no heat losses to the supports. The heat balance for this case is

$$q_s + q_r = q_n \qquad (D1)$$

where the heat stored in the cathode is q_s, the heat radiated from the cathode is q_r, and the heat added to the cathode is q_n. The heat stored in the cathode is

$$q_s = C_p M \frac{dT}{dt}$$

where C_p is the specific heat in joules per gram per ^OK, M the mass in grams, and T the temperature of the cathode in ^OK. The heat lost by radiation is

$$q_r = \epsilon \alpha k T^4$$

The heat supplied to the cathode by ohmic heating is

$$q_n = J_f^2 r$$

where k is the radiation constant in joules per square centimeter per second per $(^OK)^4$, ϵ the surface emissivity, J_f the cathode heating current in amperes; r the cathode resistance in ohms, and α the emissive area in square centimeters. Equation (1) can therefore be expanded to

$$C_p M \frac{dT}{dt} + \epsilon \alpha k T^4 = r J_f^2$$

For a small linear operating region near the steady-state cathode temperature T_o and the steady-state cathode heating current J_{F_o}, the previous equation may be represented as

$$C_p M \frac{dT}{dt} + 4\epsilon\alpha k T_o^3 T = 2rJ_f J_{f_o}$$

Taking the Laplace transform gives

$$C_p MsT(s) + 4\epsilon\alpha k T_o^3 T(s) = 2rJ_{f_o} J_f(s)$$

The transfer function can therefore be represented as

$$\frac{T(s)}{J_f(s)} = \frac{2rJ_{f_o}}{C_p Ms + 4\epsilon\alpha k T_o^3}$$

or

$$\frac{T(s)}{J_f(s)} = \frac{\dfrac{rJ_{f_o}}{2\epsilon\alpha k T_o^3}}{1 + \left(\dfrac{C_p M}{4\epsilon\alpha k T_o^3}\right)s}$$

which is in the form $G_1/(1 + \tau s)$ and corresponds to a first-order system with a time constant τ and steady-state gain G_1. The cathode-emission current is related to the temperature by the Richardson equation for normal thrustor operation. The ion beam is, in turn, a function of the cathode-emission current. For small variations about the normal operating conditions, the beam current is related to the cathode-heating current as shown in sketch (d).
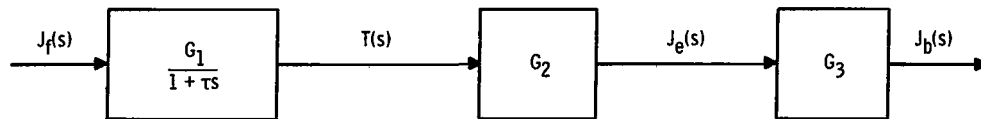
(d)

The transfer function between the beam and cathode-heating current is therefore

$$\frac{J_b(s)}{J_f(s)} = \frac{G_1 G_2 G_3}{1 + \tau s}$$

28

The time constant τ for the tantalum filament was calculated to be 0.26 second. An operating temperature of 2400° K, a specific heat C_p of 0.151 joule per gram per ^{O}K, a thermal emissivity ϵ of 0.27, and an emissive area of 0.004 square centimeter were assumed for this calculation. The break-point frequency for this time constant $(1/2\pi\tau)$ is 0.61 hertz.

REFERENCES

1. Kerslake, William R.; Wasserbauer, Joseph F.; and Margosian, Paul M.: A Mercury Electron-Bombardment Ion Thrustor Suitable for Spacecraft Station Keeping and Attitude Control. Paper No. 66-247, AIAA, Mar. 1966

2. Reader, Paul D.: Investigation of a 10-Centimeter-Diameter Electron-Bombardment Ion Rocket. NASA TN D-1163, 1962.

3. Reader, Paul D.: Experimental Performance of a 50-Centimeter Diameter Electron-Bombardment Ion Rocket. Paper No. 64-689, AIAA, 1964.

4. Reader, Paul D.; and Mickelson, William R.: Experimental Systems Studies of Large Modules and Arrays of Electrostatic Thrustors. Paper No. 64-503, AIAA, 1964.

5. Pawlik, Eugene V.: An Experimental Evaluation of Array of Three Electron-Bombardment Ion Thrustors. NASA TN D-2597, 1965.

6. Nakanishi, Shigeo; Pawlik, Eugene V.; and Baur, Charles W.: Experimental Evaluation of Steady-State Control Properties of an Electron-Bombardment Ion Thrustor. NASA TN D-2171, 1964.

7. Pawlik, Eugene V.; and Nakanishi, Shigeo: Experimental Evaluation of Size Effects on Steady-State Control Properties of Electron-Bombardment Ion Thrustor. NASA TN D-2470, 1964.

8. Stover, John B.: Effects of Thrustor Arcing on Ion Rocket System Design. Paper No. 64-682, AIAA, 1964.

9. Kerslake, William R.: Cathode Durability in the Mercury Electron-Bombardment Ion Thrustor. Paper No. 64-683, AIAA, Aug.-Sept. 1964.

10. Gille, J. C.; Pélegrin, M. J.; and Decauline, P.: Feedback Control Systems. McGraw-Hill Book Co., Inc., 1959.

11. Pawlik, Eugene V.; Margosian, Paul M.; and Staggs, John F.: A Technique for Obtaining Plasma-Sheath Configurations and Ion Optics for an Electron-Bombardment Ion Thrustor. NASA TN D-2804, 1965.

12. Guthrie, A.; and Wakerling, R. K., eds.: The Characteristics of Electrical Discharges in Magnetic Fields. McGraw-Hill Book Co. Inc., 1949.

13. D'Angelo, N.; Goeler, S. V.; and Levine, A.: Plasma Oscillations at Harmonics of the Ion Gyrofrequency. Rep. No. MATT-353, Princeton University Plasma Physics Lab., Aug. 1965.
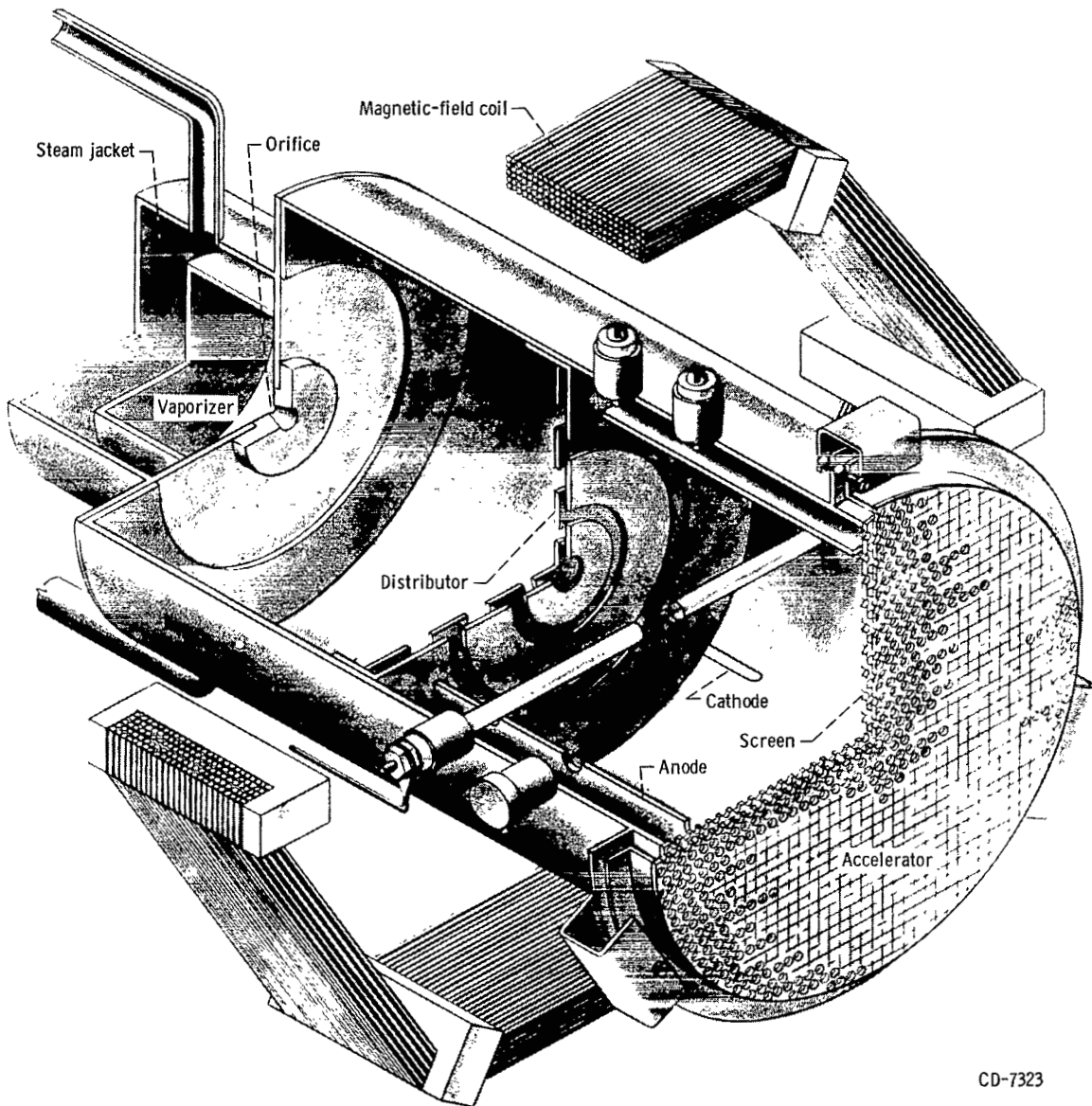
Figure 1. - Ten-centimeter-diameter electron-bombardment thrustor.

CD-7323
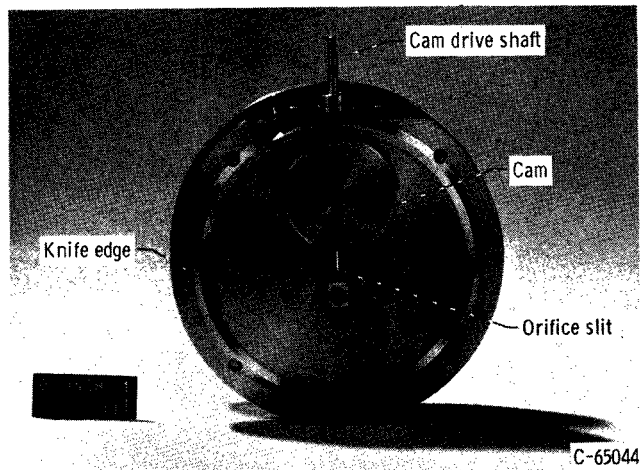
Figure 2. - Variable propellant orifice.
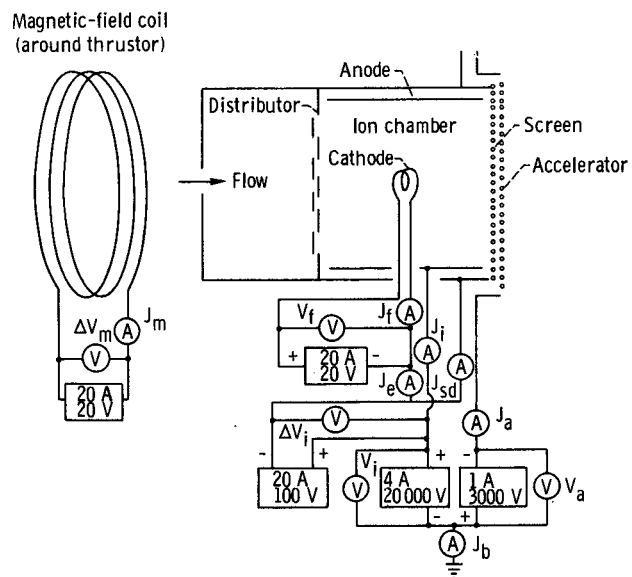
Figure 3. - Wiring diagram of ion thrustor.
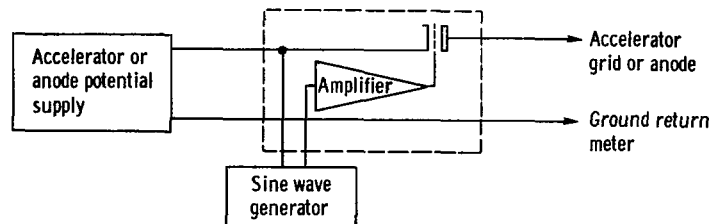
(a) Accelerator or anode potential modulator.
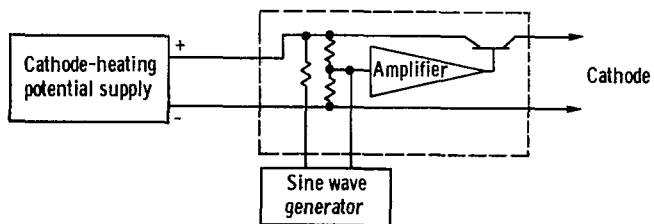
(b) Cathode-heating potential modulator.
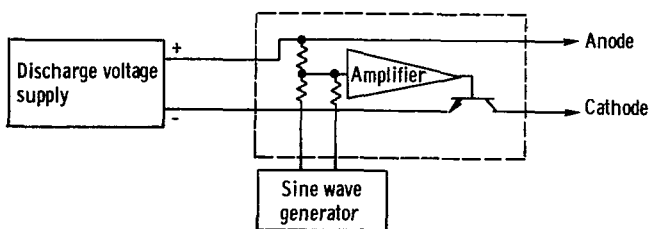
(c) Discharge voltage modulator.

Figure 4. - Thrustor parameter modulators.
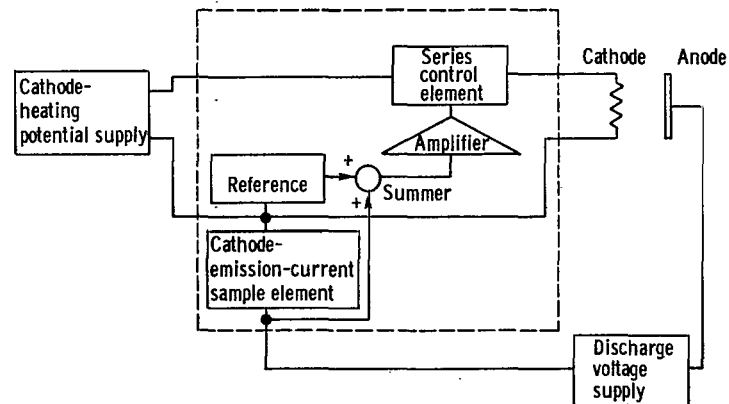
(a) Constant-emission controller.
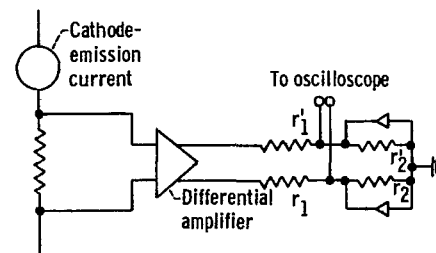
(b) Emission-current readout.

Figure 5. - Emission-current controller and readout.

Liquid-nitrogen
condenser baffle

Ion-beam
collector

12-in. valve

Thrustor

Diffusion pumps

Floor

Ejector pump

Mechanical pump
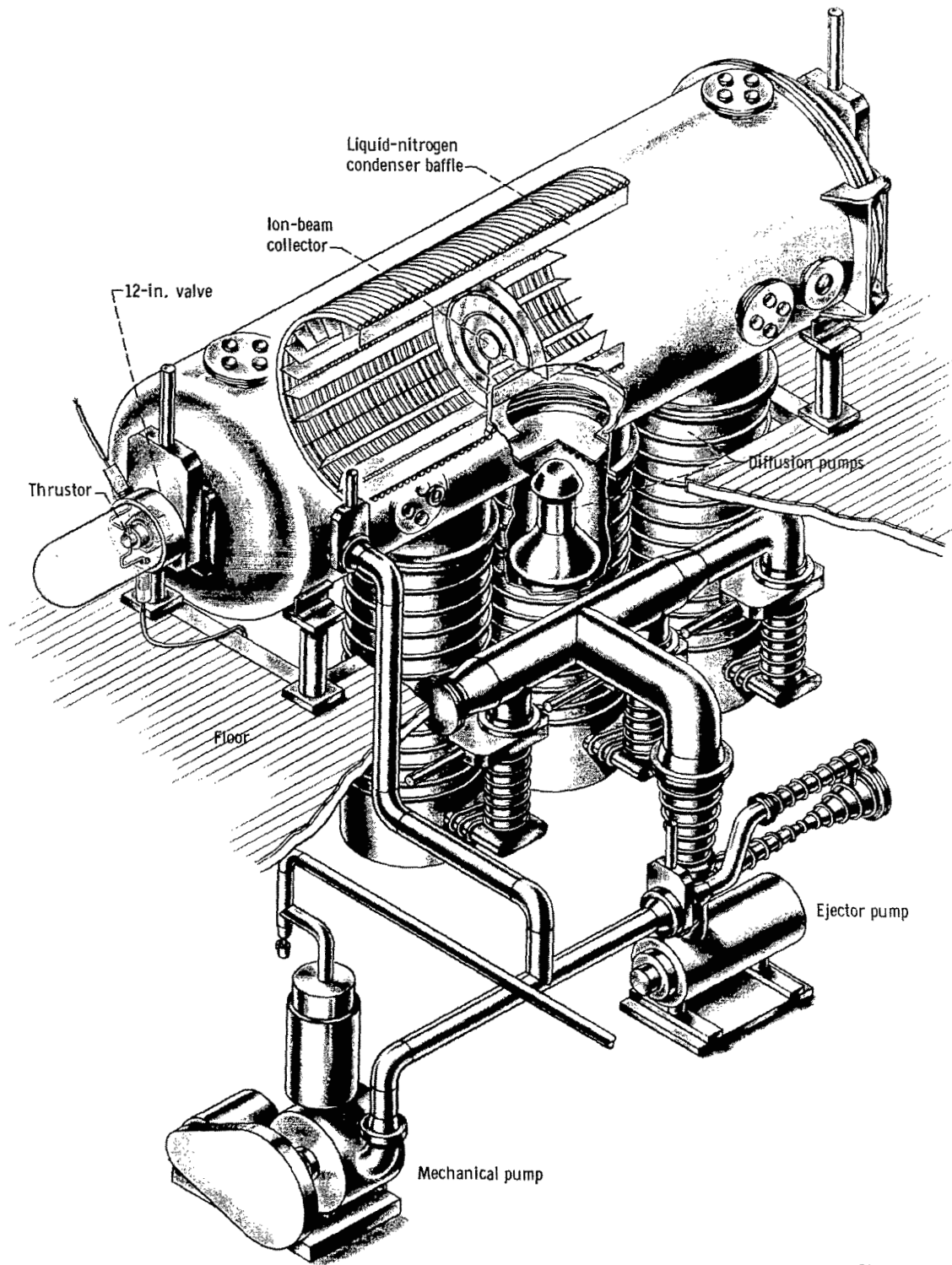
CD-9056

Figure 6. - Complete thrustor and vacuum-tank installation.
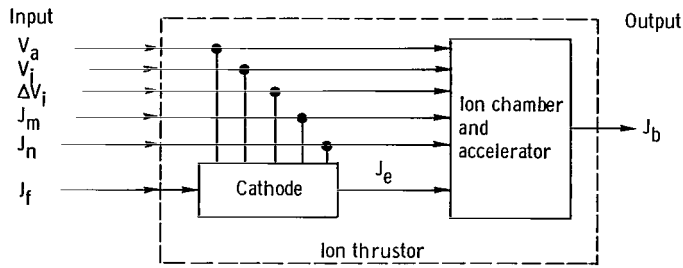
Figure 7. - Ion-thrustor block diagram.
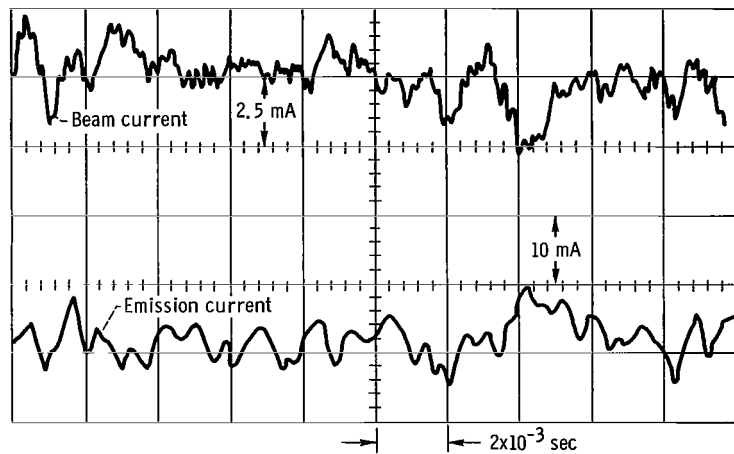
(a) Sweeprate at 2×10^{-3} second per centimeter.
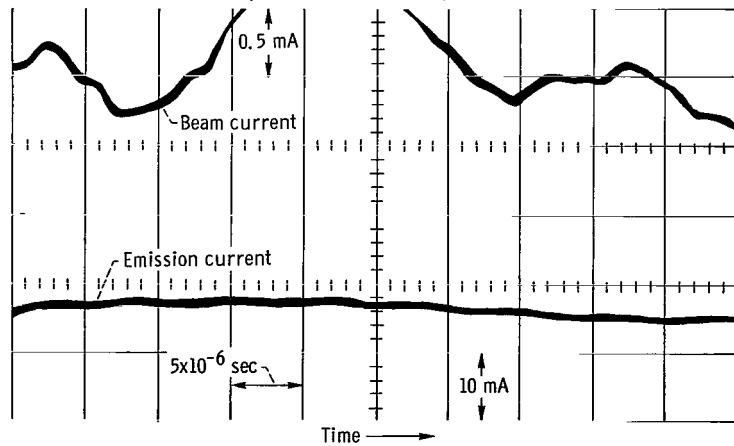
Time ⟶

(b) Sweeprate at 5×10^{-6} second per centimeter.

Figure 8. - Noise signals on beam and emission currents at normal thrustor operating conditions. Accelerator potential, -625 volts; discharge voltage, 50 volts; magnetic-field intensity, 3×10^{-3} tesla; anode potential, 2500 volts; cathode-emission current, 1.5 amperes; beam current, 0.125 amperes.
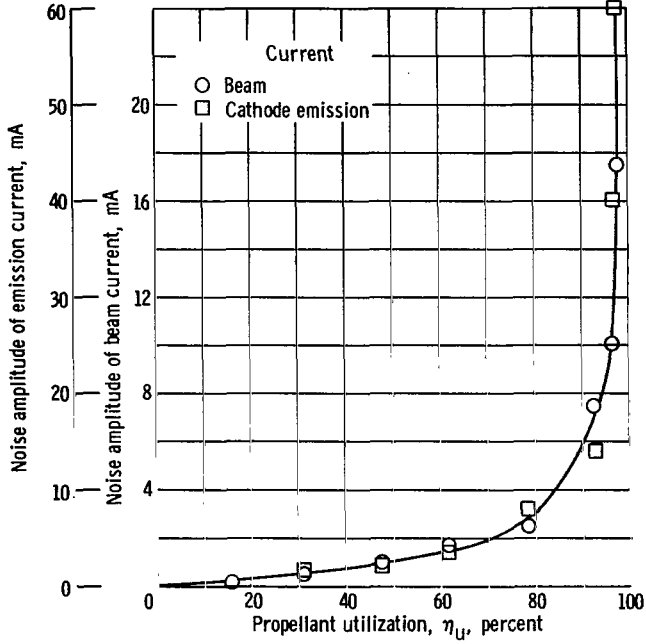
Figure 9. – Cathode-emission and ion-beam noise ampli-
tudes as functions of propellant utilization for refrac-
tory metal cathode. Accelerator potential, -625 volts;
discharge voltage, 50 volts; magnetic-field intensity,
3×10^{-3} tesla; anode potential, 2500 volts.
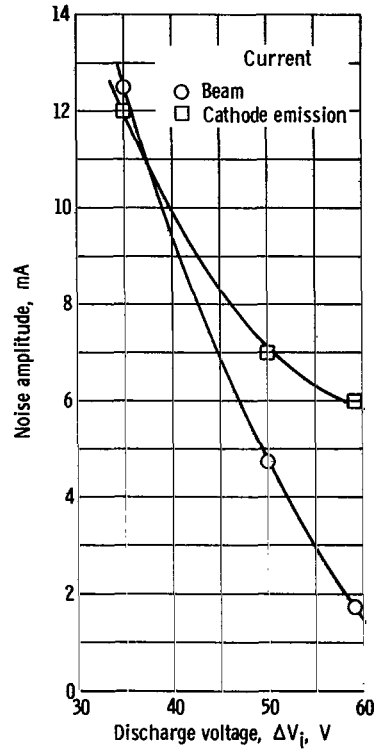
Figure 10. – Cathode-emission and
ion-beam noise amplitude as
function of discharge voltage for
refractory metal cathode. Accel-
erator potential, -625 volts;
magnetic-field intensity, 3×10^{-4}
tesla; anode potential, 2500 volts.
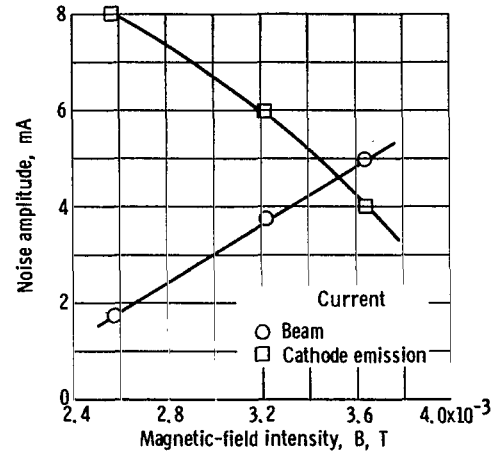
Figure 11. – Cathode-emission and ion-beam
noise amplitude as function of magnetic-
field intensity for refractory metal cathode.
Accelerator potential, -625 volts; discharge
voltage, 50 volts; anode potential, 2500 volts.
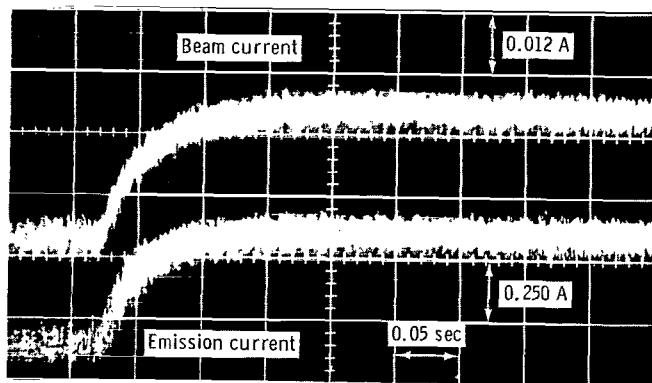
(a) Discharge voltage, 35 volts; base-point cathode-emission current, 2 amperes.
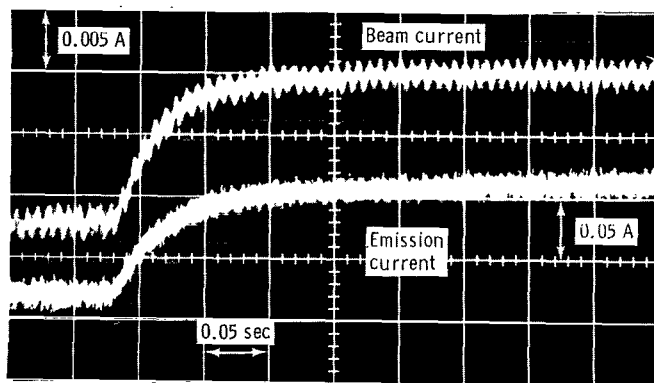
(b) Discharge voltage, 50 volts; base-point cathode-emission current, 1.51 amperes.
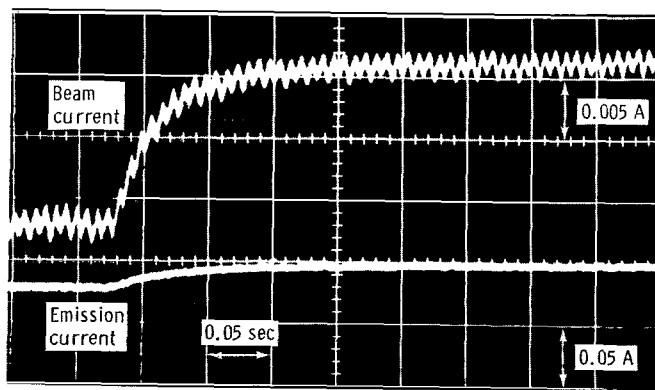
Time →

(c) Discharge voltage, 80 volts; base-point cathode-emission current, 1.30 amperes.

Figure 12. - Thrustor response to 20-percent step increase in propellant flow with a refractory metal cathode. Base-point ion-beam current, 0.125 ampere; base-point neutral propellant flow rate, 0.161 ampere; accelerator potential, -625 volts; magnetic-field intensity, 3×10^{-3} tesla; anode potential, 2500 volts.
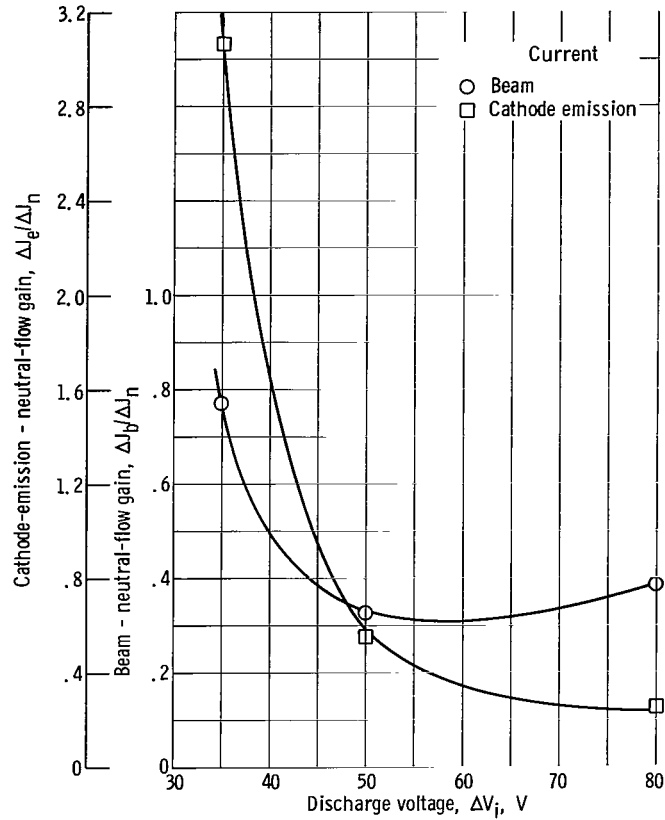
Figure 13. - Beam and cathode-emission gain to
31-milliampere equivalent step change in neu-
tral flow as function of discharge voltage for
refractory metal cathode.
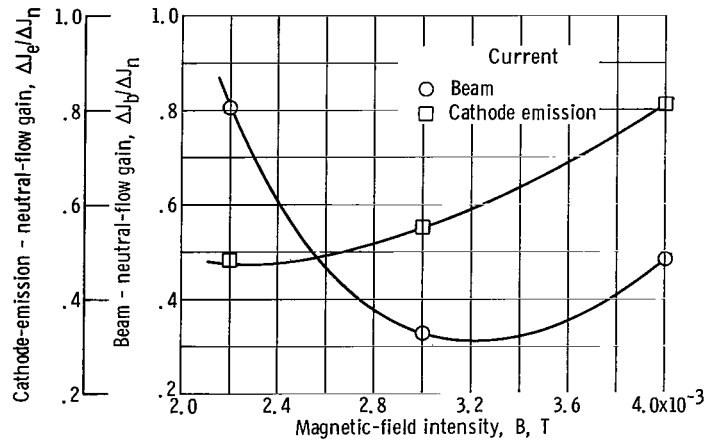
Figure 14. - Beam and cathode-emission gain to
31-milliampere equivalent step change in neu-
tral flow as function of magnetic-field intensity
for refractory metal cathode.
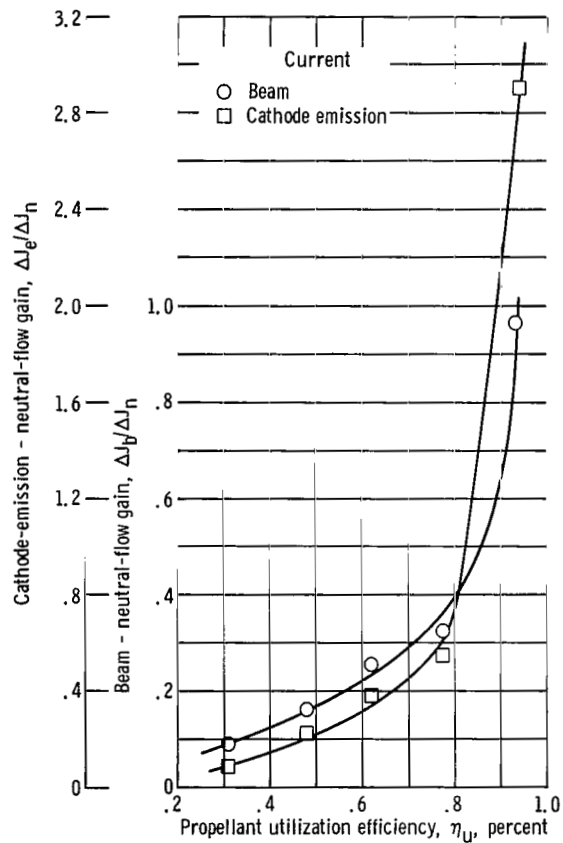
Figure 15. - Beam and cathode-emission gain to 31-milliampere equivalent step change in neutral flow as function of propellant utilization efficiency for refractory metal cathode.

(a) Magnetic-field intensity, 3×10^{-3} tesla.

Time ⟶
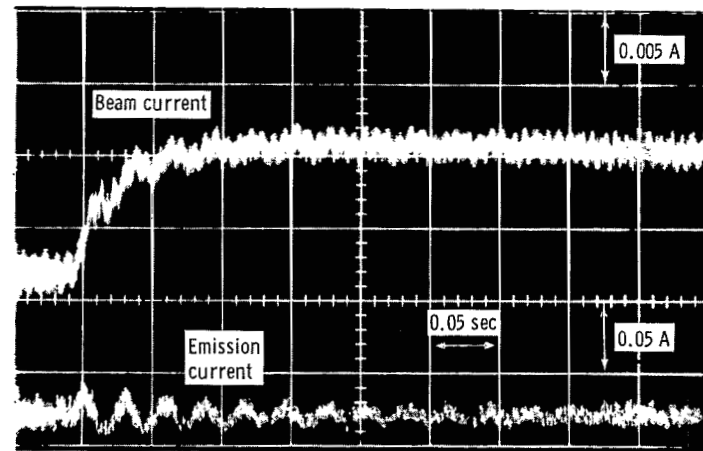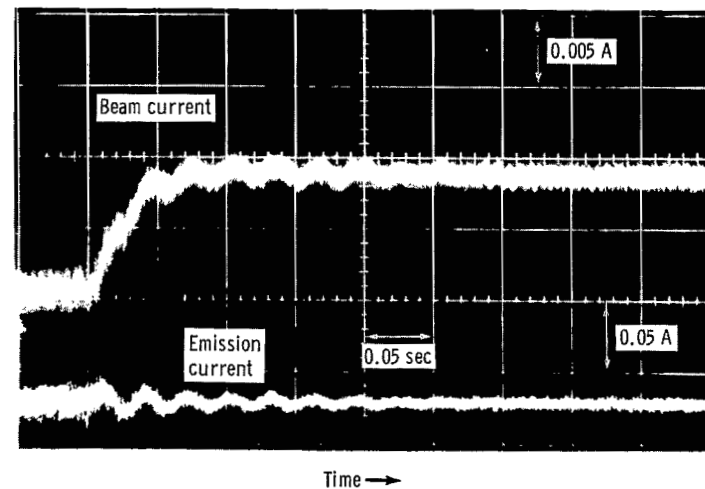
(b) Magnetic-field intensity, 4×10^{-3} tesla.

Figure 16. - Thrustor response to 20-percent step increase in propellant flow with emission controller in circuit for refractory metal cathode. Base-point ion-beam current, 0.125 ampere; base-point neutral propellant flow rate, 0.161 amperes; accelerator potential, -625 volts; discharge voltage, 50 volts; anode potential, 2500 volts; cathode-emission current, 1.5 amperes.
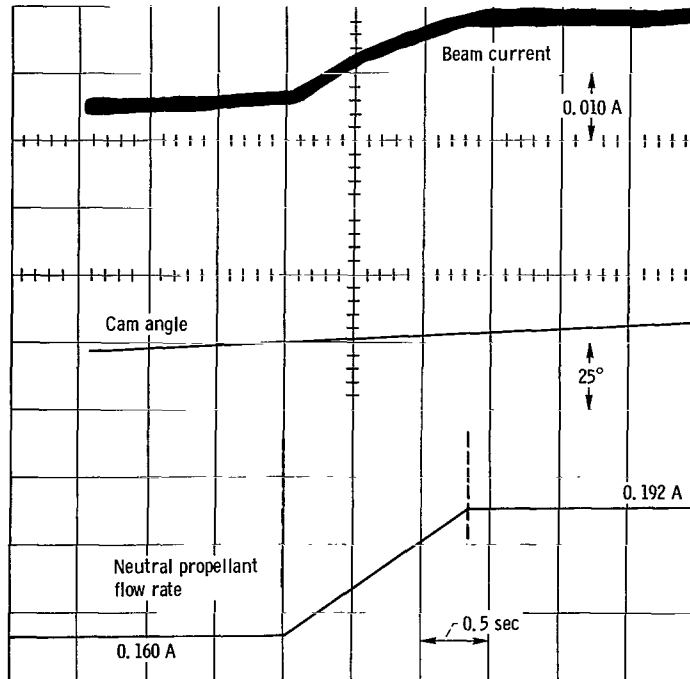
(a) Determination of open and closed positions of variable area orifice.
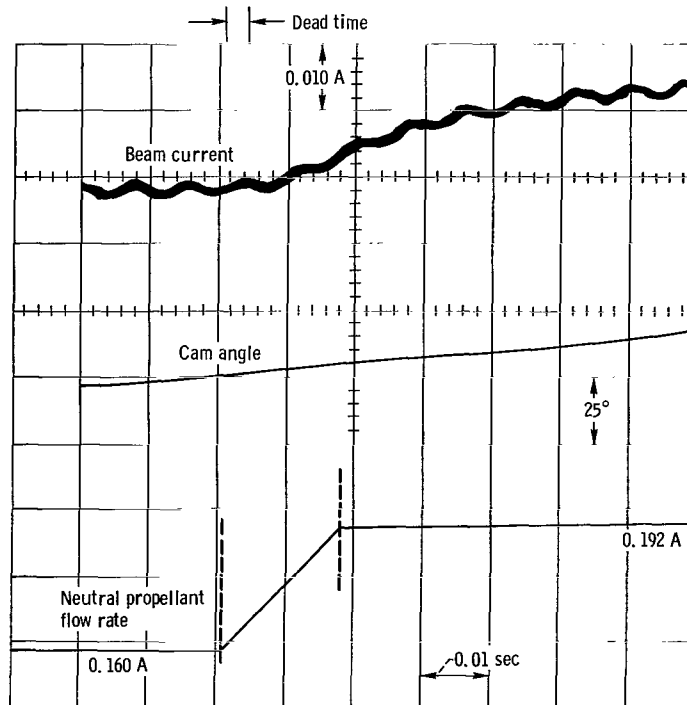
(b) Determination of time lag between neutral propellant flow rate and ion-beam current.

Figure 17. - Beam current and orifice cam position traces used to determine time lags for refractory metal cathode. Base-point ion-beam current, 0.125 ampere; accelerator potential, -625 volts; discharge voltage, 50 volts; magnetic-field intensity, 3×10^{-3} tesla; anode potential, 2500 volts.

Ion-beam current, J_b, mA

Auto cathode

Auto cathode

Discharge
voltage,
ΔV_i

30
35
40
45
50
55

Solid symbols denote initial
step change values
Open symbols denote other
step change values

Solid symbols denote final
step change values
Open symbols denote other
step change values

Cathode-emission current, J_e, A

(a) Neutral propellant flow rate, 0.161 ampere.

(b) Neutral propellant flow rate, 0.192 ampere.
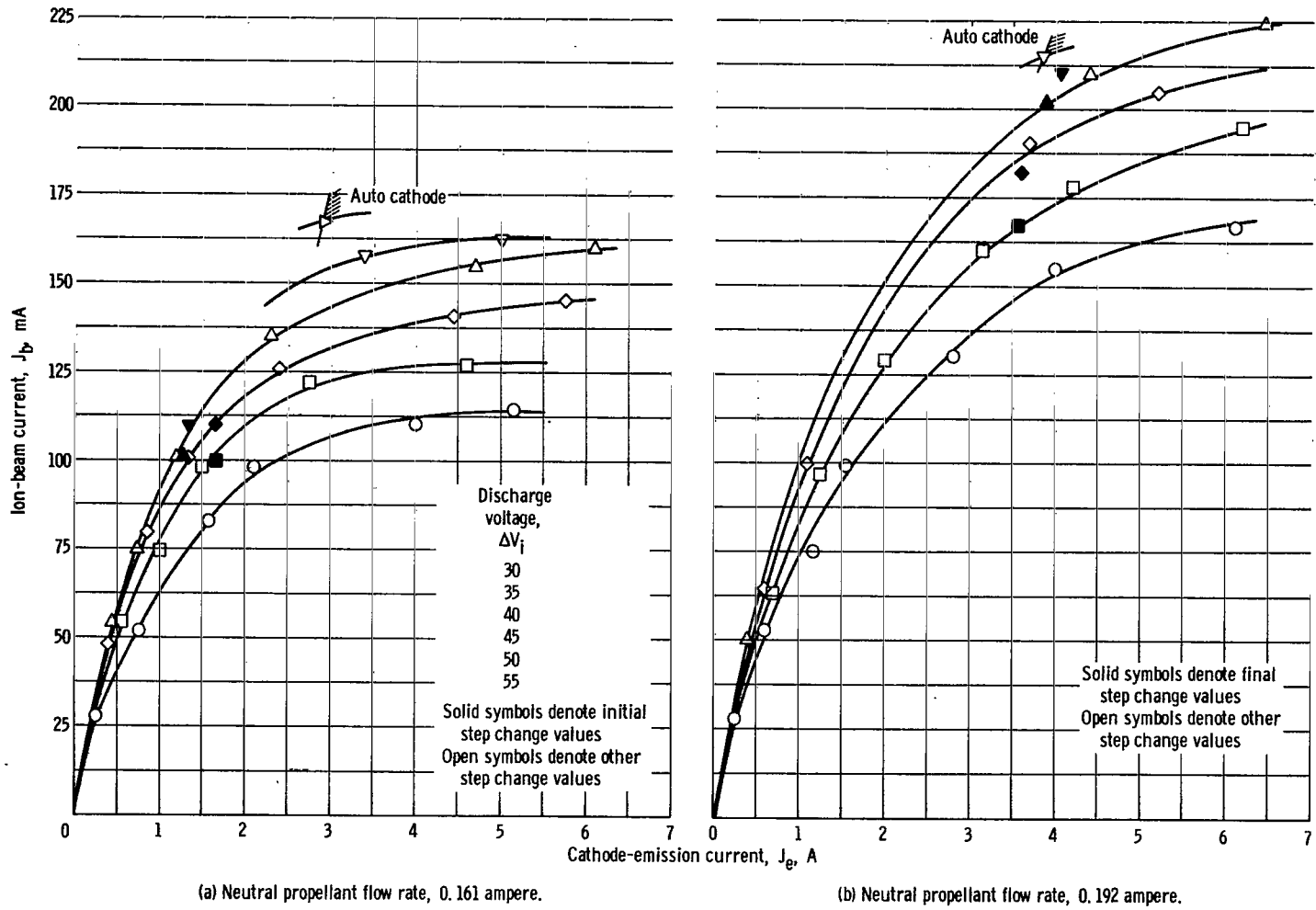
Figure 18. – Ion-beam – cathode-emission-current characteristics for oxide-coated cathode. Accelerator potential, -625 volts; magnetic-field intensity, 3×10^{-3} tesla; anode potential, 2500 volts.
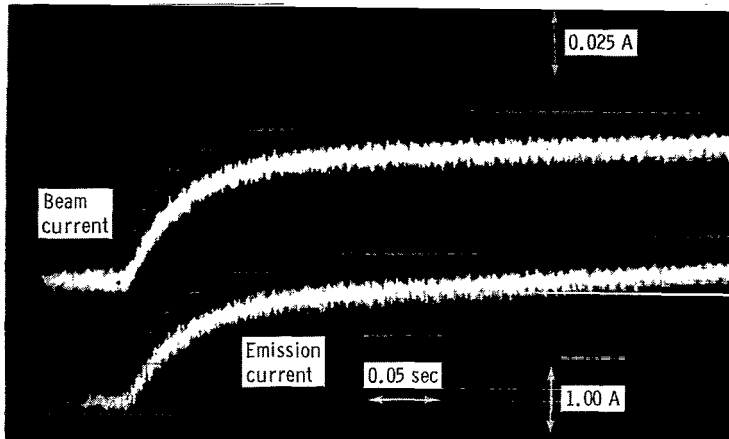
(a) Sweeprate, 0.050 second per centimeter.
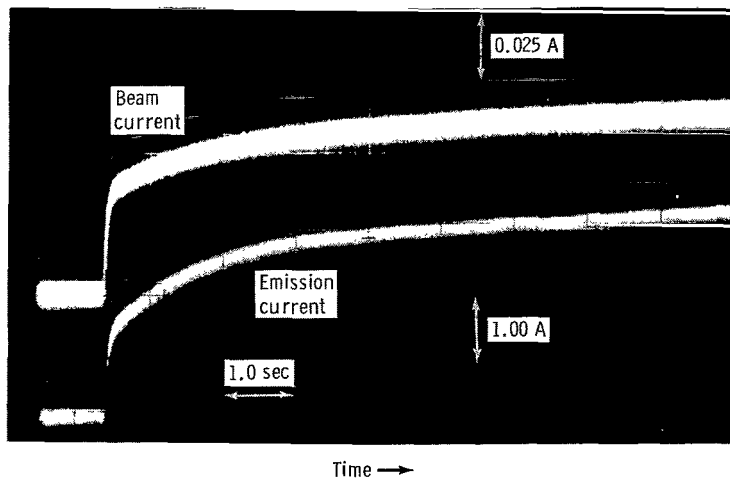
Time →

(b) Sweeprate, 1.00 second per centimeter.

Figure 19. - Response of oxide-coated cathode to 20-percent step increase in propellant flow. Base-point ion-beam current, 0.098 ampere; base-point cathode emission current, 1.65 ampere; base-point neutral propellant flow rate, 0.161 ampere; accelerator potential, -625 volts; discharge voltage, 35 volts; magnetic-field intensity, 3×10^{-3} tesla; anode potential, 2500 volts.
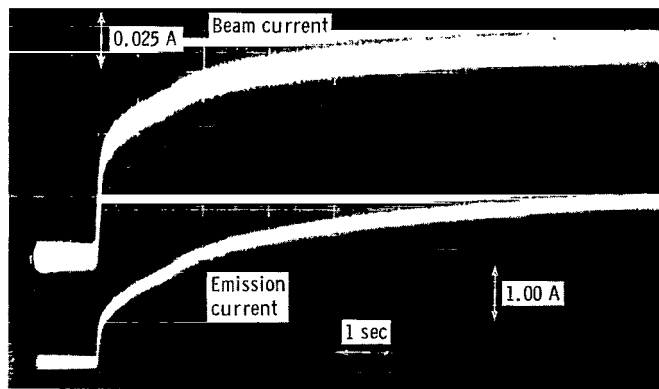
(a) Base-point ion-beam current, 0.110 ampere; base-point cathode-emission current, 1.65 amperes; discharge voltage, 40 volts.
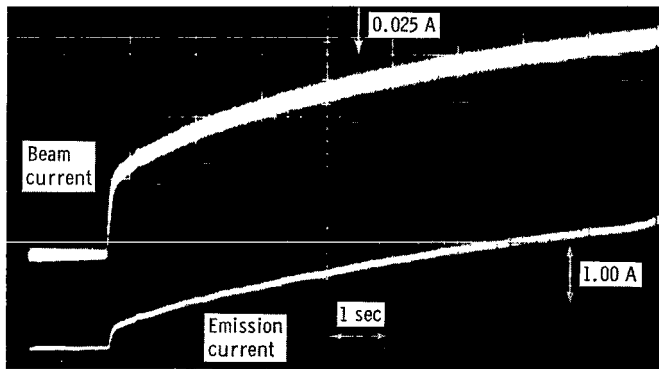
(b) Base-point ion-beam current, 0.110 ampere; base-point cathode-emission current, 1.30 amperes; discharge voltage, 45 volts.
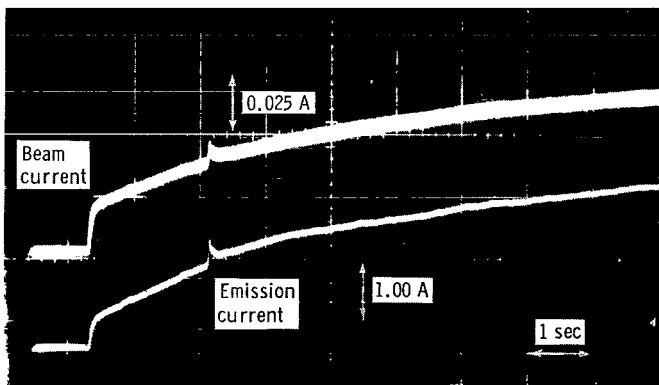
Time →

(c) Base-point ion-beam current, 0.101 ampere; base-point cathode-emission current, 1.30 amperes; discharge voltage, 50 volts.

Figure 20. - Response of oxide-coated cathode at various levels of discharge voltage to 20-percent step change in propellant flow. Initial neutral propellant flow rate, 0.161 ampere; accelerator potential, -625 volts; magnetic-field intensity, 3×10^{-3} tesla; anode potential, 2500 volts; time, 1 second per centimeter.
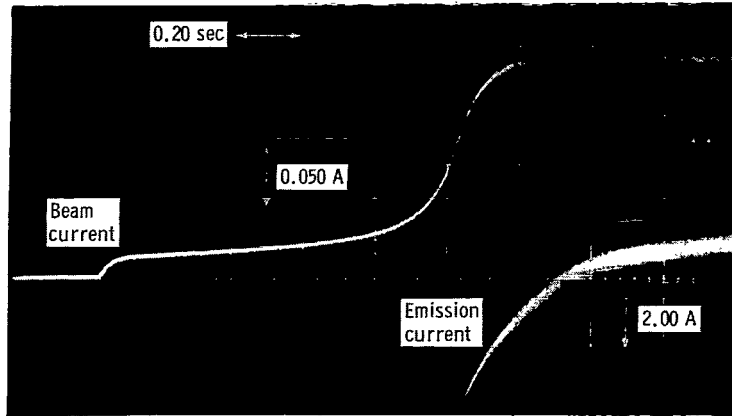
(a) Sweeprate, 0.20 second per centimeter.
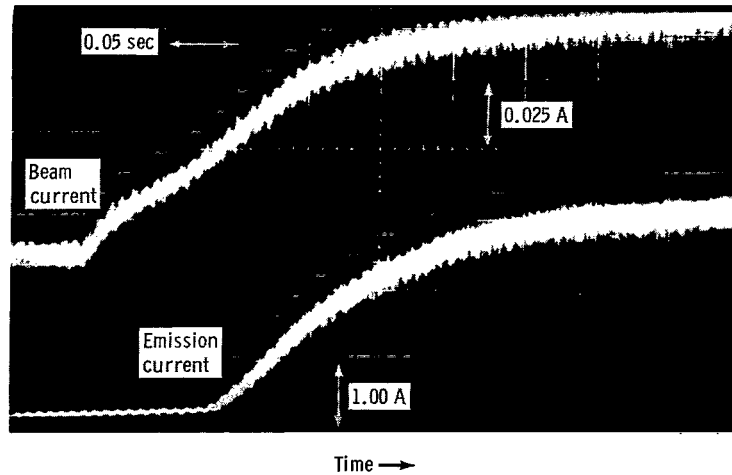
Time ⟶

(b) Sweeprate, 0.05 second per centimeter.

Figure 21. – Response of oxide-coated cathode to 20-percent step change in propellant flow. Base-point ion-beam current, 0.050 ampere; base-point cathode-emission current, 0.45 ampere; accelerator potential, -625 volts; discharge voltage, 45 volts; anode potential, 2500 volts.
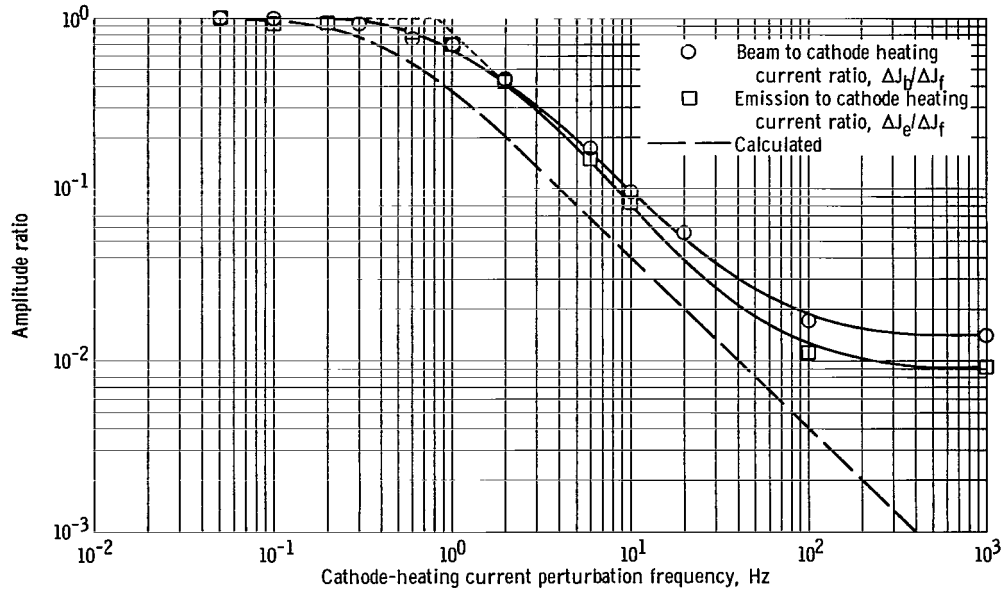
Figure 22. – Amplitude response of beam and emission currents to cathode heating current with refractory metal cathode.
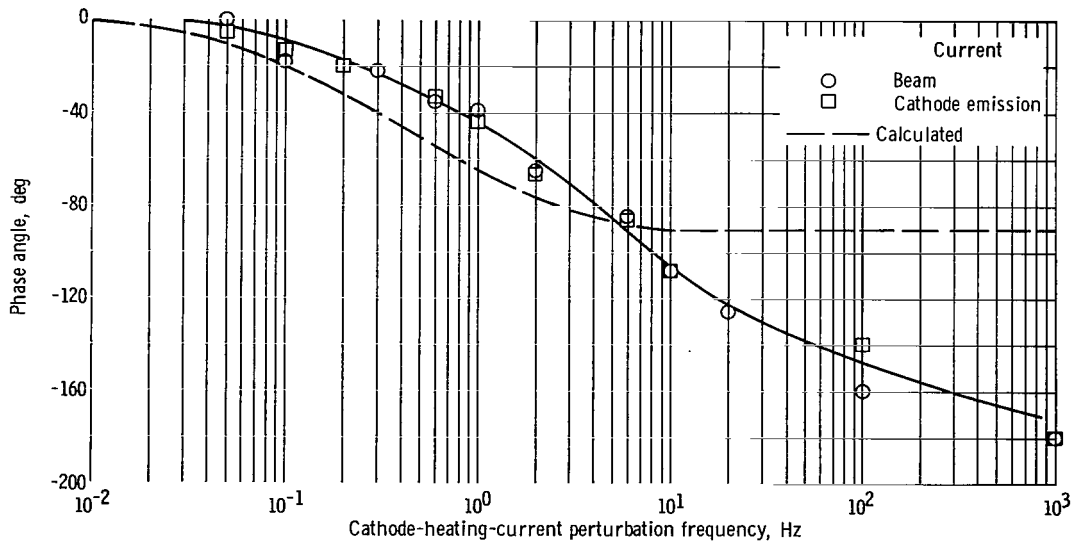
Figure 23. – Phase response of beam and emission current to cathode-heating current with refractory metal cathode.
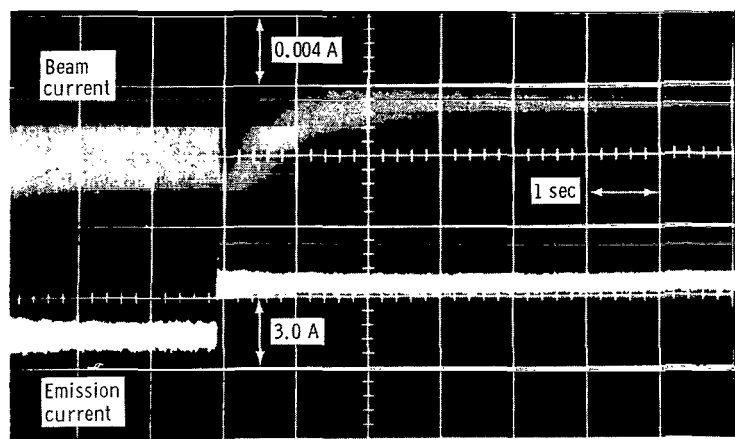
(a) Increase in cathode-heating current.
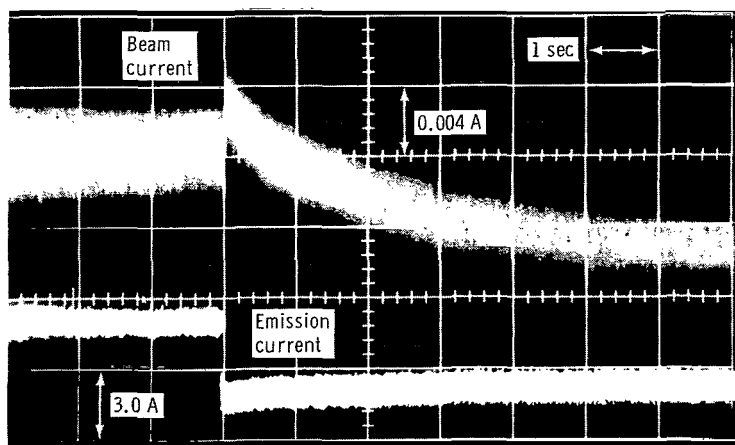
Time ⟶

(b) Decrease in cathode-heating current.

Figure 24. - Response of beam current to step change in cathode-heating current for an oxide-coated cathode.
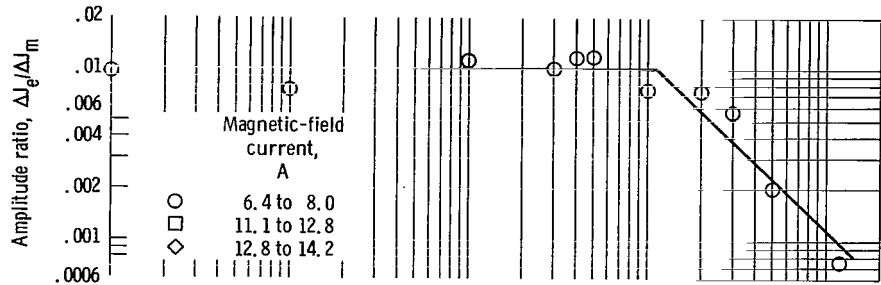
(a) Cathode-emission current.
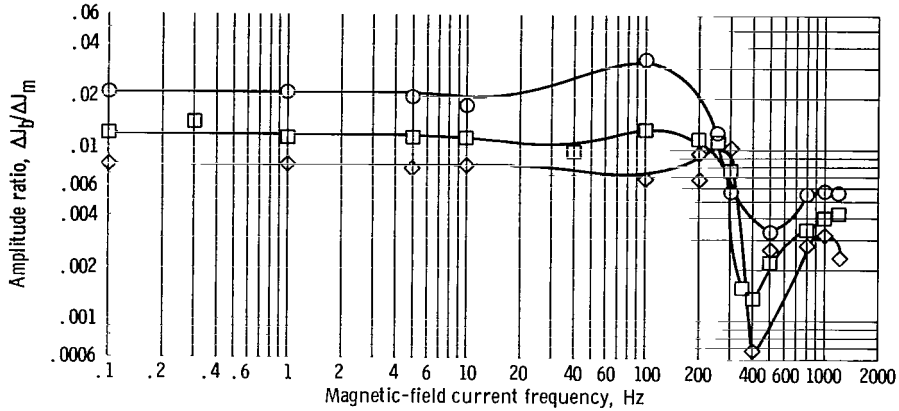
(b) Ion-beam current.

Figure 25. - Amplitude response of thrustor magnetic-field current. Steady-state conditions, 1 ampere equals 4×10^{-4} tesla.
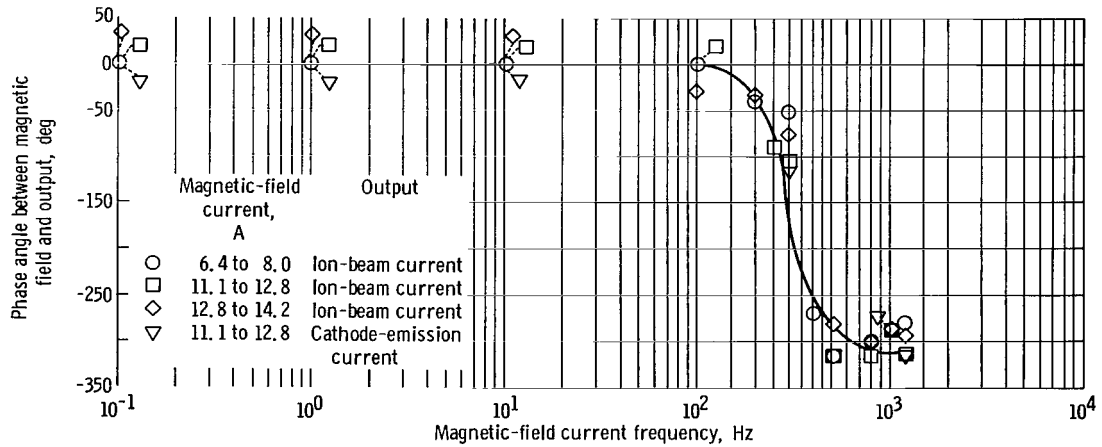
Figure 26. - Phase angle response of beam and cathode emission current to magnetic-field current.

(a) Discharge on.

Time ⟶
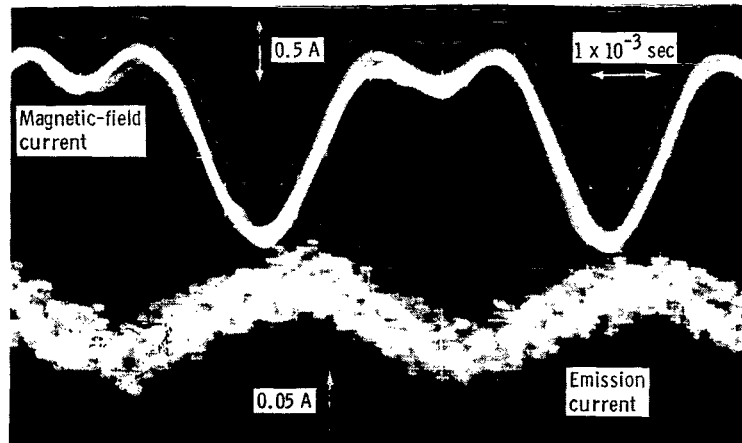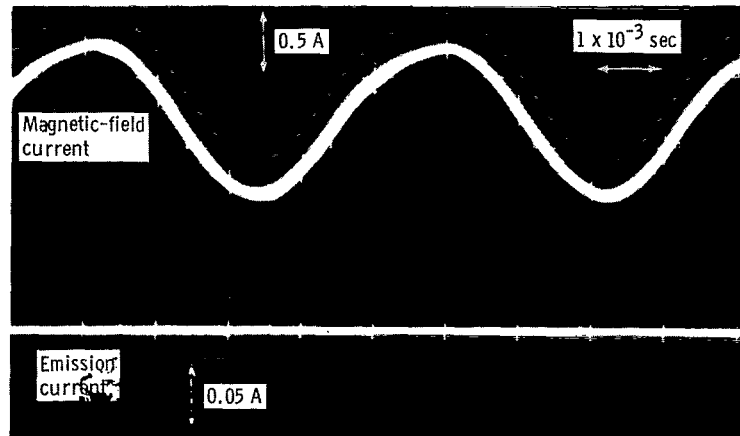
(b) Discharge off.

Figure 27. - Loading effect of ion chamber on magnetic-field power supply. Magnetic-field intensity, 3×10^{-3} telsa; magnetic-field current frequency, 200 hertz.

(a) Ion-beam current.

(b) Cathode-emission current.
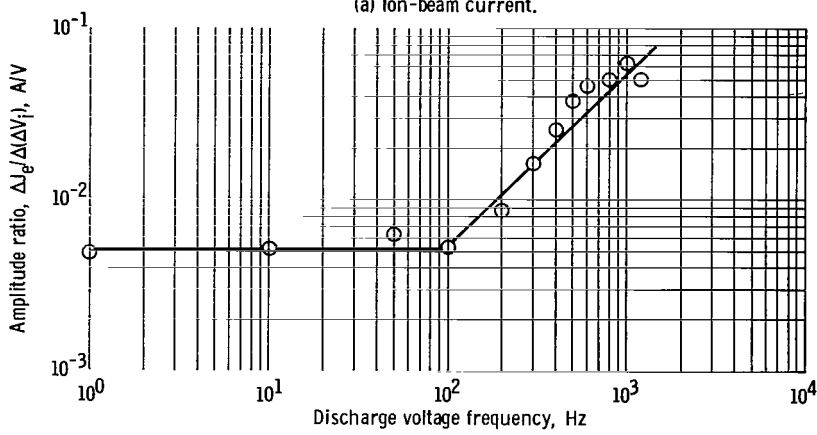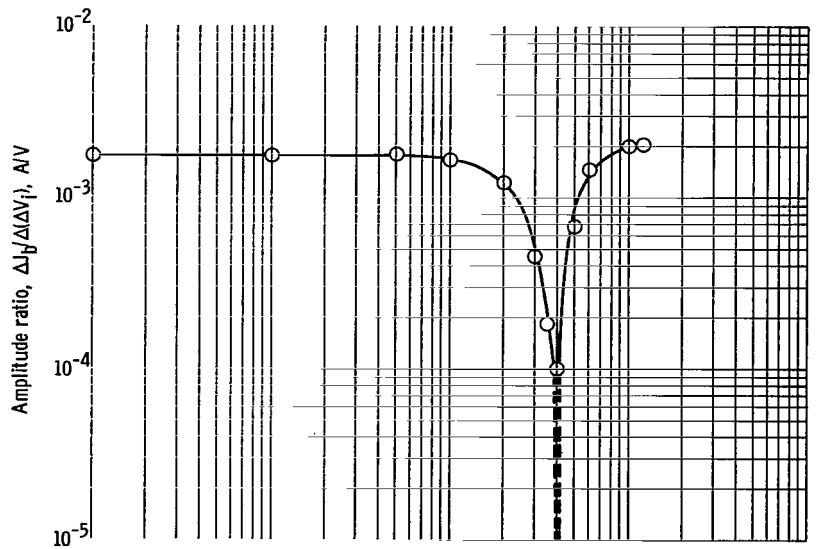
Figure 28. – Amplitude response of thrystor to discharge voltage for refractory metal cathode.
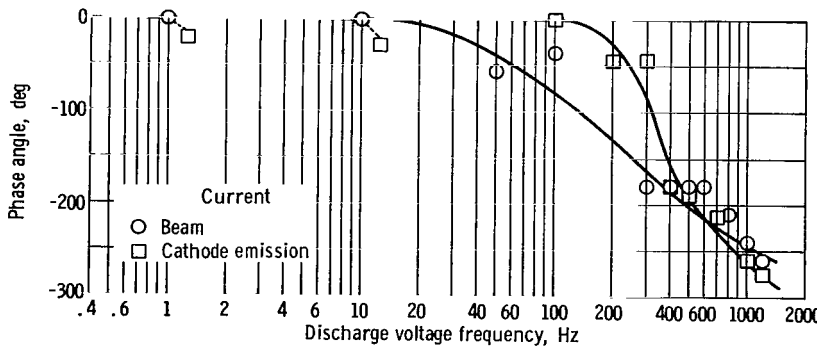
Figure 29. – Phase response of beam and emission currents to discharge voltage for refractory metal cathode.
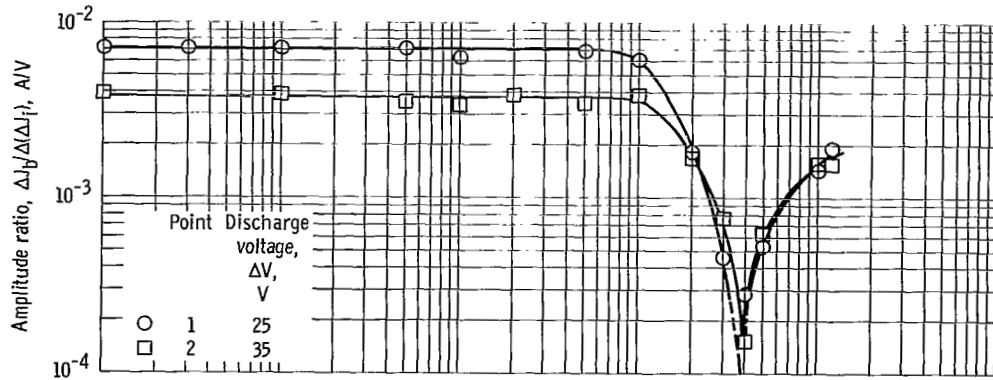
(a) Ion-beam current.
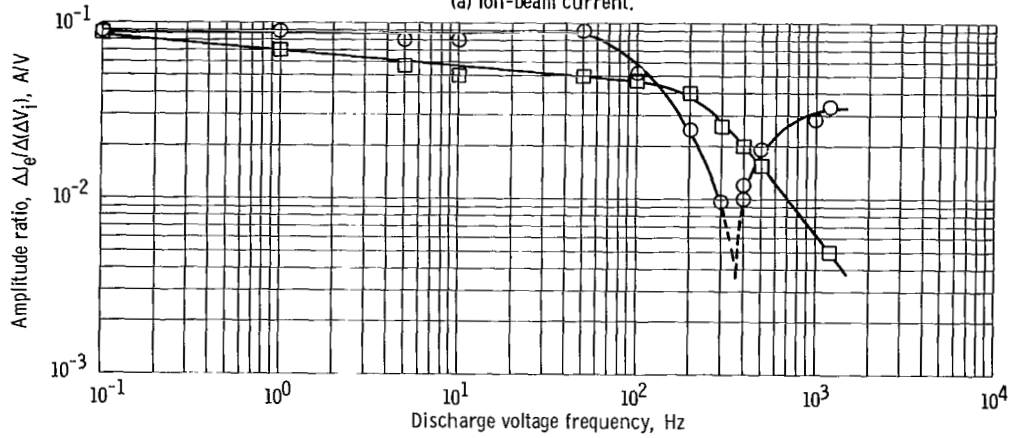
(b) Cathode-emission current.

Figure 30. – Amplitude response of thrustor to discharge voltage for oxide-coated cathode.
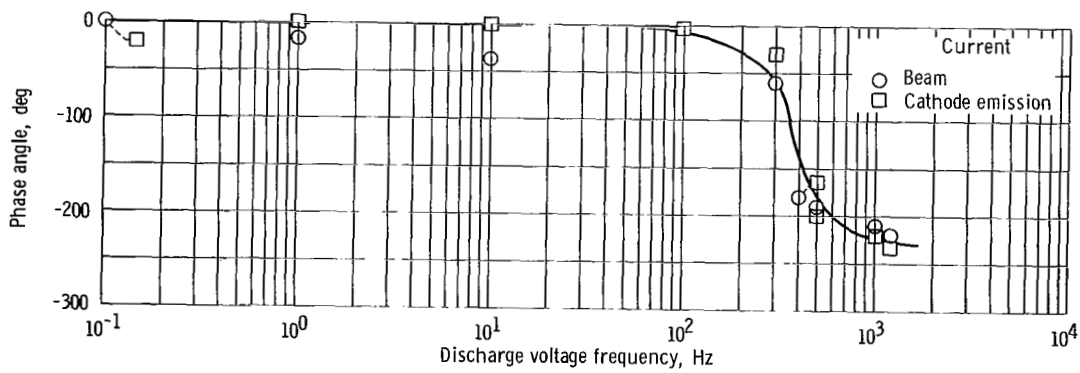

Figure 31. – Phase response of beam and emission currents to discharge voltage for oxide-coated cathode.

50
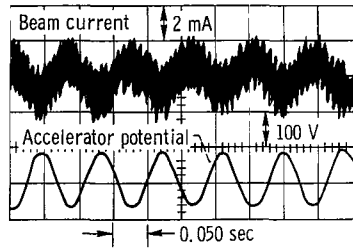
(a) Beam current response and accelerator potential waveform. Direct-current level of accelerator potential, -730 volts; frequency, 10 hertz.
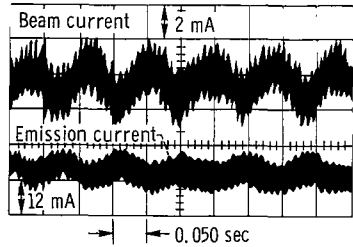
(b) Beam and emission current response. Frequency, 10 hertz.
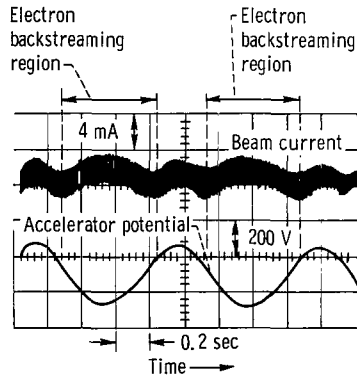
(c) Beam current response and accelerator potential waveform. Direct-current level of accelerator potential, -720 volts; frequency, 1 hertz.

Figure 32. - Thrustor response to changes in accelerator potential with refractory metal cathode.
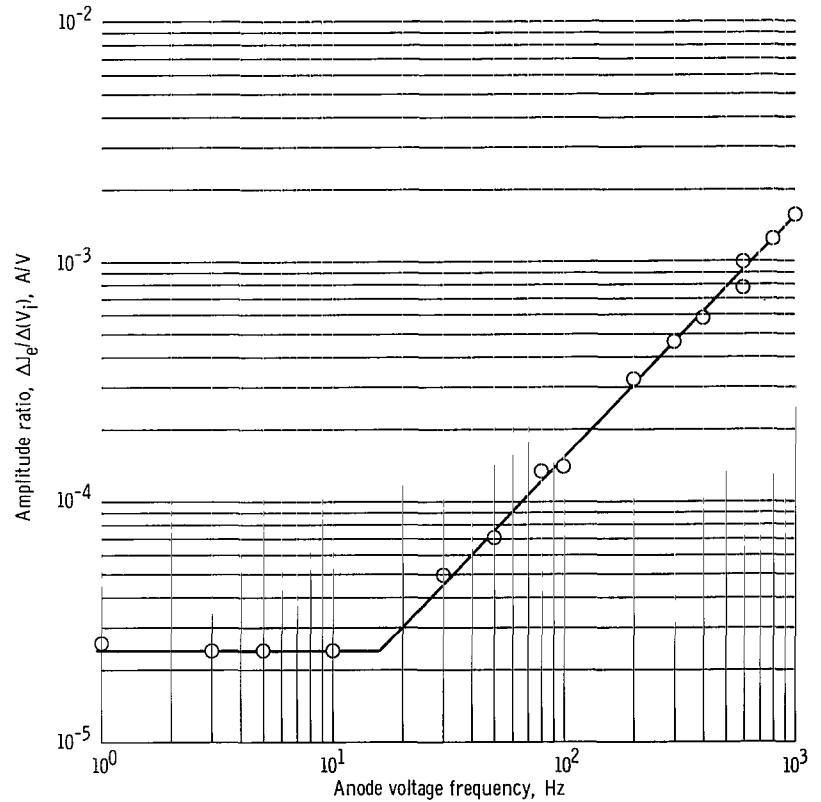

Figure 33. - Amplitude response of emission current to anode voltage.

"The aeronautical and space activities of the United States shall be conducted so as to contribute . . . to the expansion of human knowledge of phenomena in the atmosphere and space. The Administration shall provide for the widest practicable and appropriate dissemination of information concerning its activities and the results thereof."

—NATIONAL AERONAUTICS AND SPACE ACT OF 1958

NASA SCIENTIFIC AND TECHNICAL PUBLICATIONS

TECHNICAL REPORTS: Scientific and technical information considered important, complete, and a lasting contribution to existing knowledge.

TECHNICAL NOTES: Information less broad in scope but nevertheless of importance as a contribution to existing knowledge.

TECHNICAL MEMORANDUMS: Information receiving limited distribution because of preliminary data, security classification, or other reasons.

CONTRACTOR REPORTS: Scientific and technical information generated under a NASA contract or grant and considered an important contribution to existing knowledge.

TECHNICAL TRANSLATIONS: Information published in a foreign language considered to merit NASA distribution in English.

SPECIAL PUBLICATIONS: Information derived from or of value to NASA activities. Publications include conference proceedings, monographs, data compilations, handbooks, sourcebooks, and special bibliographies.

TECHNOLOGY UTILIZATION PUBLICATIONS: Information on technology used by NASA that may be of particular interest in commercial and other non-aerospace applications. Publications include Tech Briefs, Technology Utilization Reports and Notes, and Technology Surveys.

Details on the availability of these publications may be obtained from:

SCIENTIFIC AND TECHNICAL INFORMATION DIVISION

NATIONAL AERONAUTICS AND SPACE ADMINISTRATION
Washington, D.C. 20546